*J. Fluid Mech.* (2003), *vol.* 477, *pp.* 51–88.  
DOI: 10.1017/S0022112002003075 Printed in the United Kingdom

# The 1:2 mode interaction in exactly counter-rotating von Kármán swirling flow

By C. NORE[1,2], L. S. TUCKERMAN[2], O. DAUBE[3] AND S. XIN[1,2]

[1]Université Paris XI, Département de Physique, 91405 Orsay cedex, France

[2]Laboratoire d'Informatique pour la Mécanique et les Sciences de l'Ingénieur, CNRS, BP 133, 91403 Orsay cedex, France

[3]Université d'Evry Val d'Essonne, 40 rue du Pelvoux, 91020 Evry cedex, France

(Received 3 January 2002 and in revised form 11 September 2002)

The flow produced in an enclosed cylinder of height-to-radius ratio of two by the counter-rotation of the top and bottom disks is numerically investigated. When the Reynolds number based on cylinder radius and disk rotation is increased, the axisymmetric basic state loses stability and different complex flows appear successively: steady states with an azimuthal wavenumber of 1; travelling waves; near-heteroclinic cycles; and steady states with an azimuthal wavenumber of 2. This scenario is understood in a dynamical system context as being due to a nearly codimension-two bifurcation in the presence of $O(2)$ symmetry. A bifurcation diagram is determined, together with the most dangerous eigenvalues as functions of the Reynolds number. Two distinct types of near-heteroclinic cycles are observed, with either two or four bursts per cycle. The physical mechanism for the primary instability could be the Kelvin–Helmholtz instability of the equatorial azimuthal shear layer of the basic state.

## 1. Introduction

The flow produced in an enclosed cylinder driven by the rotation of the upper and lower bounding disks has long been the focus of theoretical, experimental, and numerical investigation. These flows, first studied by Batchelor (1951), were given the name of von Kármán swirling flows by Zandbergen & Dijkstra (1987) and occur frequently in geophysical and in industrial applications, notably turbines. There is a vast literature on von Kármán flows; here, we confine ourselves to citing mainly recent articles (i.e. after 1998), when non-axisymmetric simulations began to be feasible.

The flow depends strongly on the height-to-radius aspect ratio $\Gamma$, as well as on the ratio $s$ of the angular velocities of the upper and lower disks. Rotating flows with $\Gamma \ll 1$ and $s = 0$ are called rotor–stator flows. These flows are characterized by the coexistence of Ekman and Bödewadt boundary layers, in the neighbourhood of the rotating and the stationary disk, respectively (e.g. Schouveiler, Le Gal & Chauve 1998, 2001; Gauthier, Gondret & Rabaud 1999). Above the threshold, the axisymmetric basic state loses stability to circular patterns of axisymmetric vortices and spiral waves. Circular patterns have been investigated with axisymmetric numerical simulations (Lopez 1996; Cousin-Rittemard, Daube & Le Quéré 1998; Daube *et al.* 2001) whereas spiral waves require three-dimensional computations (Serre *et al.* 2001; Serre, Crespo del Arco & Bontoux 2001). Schouveiler *et al.* (2001) studied experimentally

the transitions to circles and spiral waves characterized by a positive orientation with respect to the rotating disk. Gauthier *et al.* (2002) showed that the co-rotating and the weakly counter-rotating cases give instabilities similar to those in the rotor–stator case, whereas a higher counter-rotation leads to a new spiral pattern whose orientation is negative with respect to the faster disk.

For $\Gamma = O(1)$, the case of a fixed top lid ($s = 0$) is also the most widely studied configuration, both experimentally (Vogel 1968; Escudier 1984; Spohn, Mory & Hopfinger 1998; Stevens, Lopez & Cantwell 1999) and numerically (Lugt & Abboud 1987; Daube & Sorensen 1989; Lopez 1990; Gelfgat, Bar-Yoseph & Solan 1996 *a*, *b*; Lopez, Marques & Sanchez 2001). The main reason for this interest in the axisymmetric case is the possible onset of recirculation zones on the cylinder axis. This was related by Escudier (1984) to vortex breakdown phenomena characterized by reversed axial flow in the central vortex core. In the range of parameters studied by Escudier, no significant departure from axisymmetry was observed, thereby justifying the assumption of axisymmetry of early numerical studies. Gelfgat *et al.* (1996*a*) and Lopez (1998) have surveyed the axisymmetric flow as a function of positive and negative $s$.

With the development of more powerful computers, attention has turned to the three-dimensional symmetry breaking of the basic state (Sotiropoulos & Ventikos 1998, 2001; Blackburn & Lopez 2000; Gelfgat, Bar-Yoseph & Solan 2001; Marques & Lopez 2001; Blackburn & Lopez 2002; Marques, Lopez & Shen 2002; Lopez *et al.* 2002). Gelfgat *et al.* (2001) performed a linear stability analysis of the steady axisymmetric base flow in the range $\Gamma \in [1, 3.5]$ and found that, for $1.63 \leqslant \Gamma \leqslant 2.76$, the first bifurcation is axisymmetric. For different values of $\Gamma$, many distinct scenarios have been observed in nonlinear regimes: transition from bubble vortex breakdown to a precessing columnar vortex core (Sotiropoulos & Ventikos 1998), coexistence of structures with azimuthal wavenumbers 1 and 4 (Marques & Lopez 2001), double Hopf bifurcation between azimuthal wavenumbers 0 and 2 (Marques *et al.* 2002), periodic or quasi-periodic solutions with modulated rotating waves (Blackburn & Lopez 2000, 2002). Lopez *et al.* (2002) have varied $s$ between 0 and $-0.8$, for $\Gamma = 0.5$ and have observed rotating waves with azimuthal wavenumbers 4 and 5, as well as more complicated dynamics.

Turbulence in von Kármán flows with $\Gamma = O(1)$ and $s = -1$ has been the subject of a number of experimental investigations, primarily because this system is maximally efficient in forcing turbulence when the disks are exactly counter-rotating. Using different working fluids such as air (Labbe, Pinton & Fauve 1996), water (Cadot, Douady & Couder 1995), helium (Belin *et al.* 1996), gallium (Odier, Pinton & Fauve 1998) and sodium (Marié *et al.* 2000), the counter-rotating set-up can reach very high Reynolds numbers, up to $Re \simeq 10^7$. Turbulence in such flows has been studied from a statistical viewpoint, focusing on probability density functions of the velocity increments or pressure signal, and Kolmogorov scalings and departure from them. Other studies have had a mechanistic viewpoint, focusing on tube-like high-vorticity regions on a small-vorticity sea background, and coherent structures such as small-scale worms (Belin *et al.* 1996) and integral-scale tubes (Douady, Couder & Brachet 1991). Even in these highly turbulent flows, long-lived vortices were observed which could be 'ghosts' of the coherent structures existing for smaller Reynolds numbers (Cadot 1995; La Porta *et al.* 2000).

Nonetheless, the early stages of transition for parameter values $\Gamma = O(1)$ and $s = -1$ have not been previously considered. The main purpose of this paper is to study the first steps towards turbulence of the counter-rotating von Kármán swirling

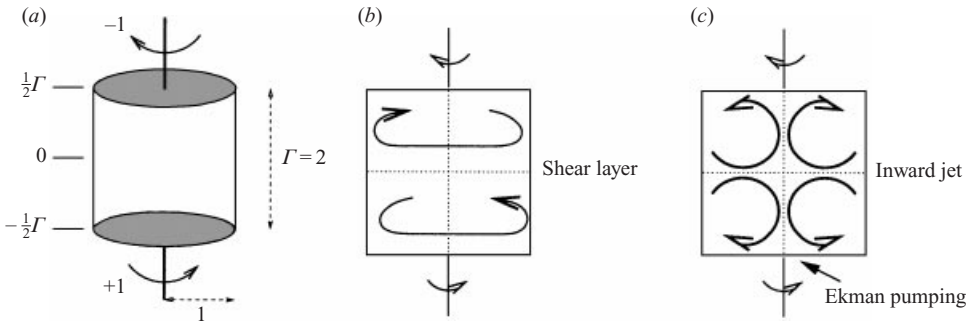


FIGURE 1. (*a*) Schematic diagram of the flow configuration in non-dimensionalized units. (*b*) Shear layer and (*c*) recirculation zones due to Ekman pumping.

flow. The outline of the paper is as follows: in § 2, the problem is formulated, along with its symmetries and associated normal form; § 3 summarizes the numerical techniques. In § 4, we report the thresholds for bifurcations from the basic axisymmetric state; in § 5, we describe in detail the sequence of steady and time-dependent states observed, placing it in the context of the normal form. In § 6, we discuss a possible physical mechanism for the instability; § 7 contains our conclusion.

## 2. Formulation of the problem

### 2.1. *Geometry*

We consider in this paper the flow of an incompressible fluid of kinematic viscosity $\nu$, in a cylindrical cavity of radius $R$ and height $H$. The motion is generated by rotation of the upper and lower disks at constant angular velocity $\Omega_{up}$ and $\Omega_{low}$, respectively. The flow thus depends on three non-dimensional parameters. Using $R$ as the length scale and $\Omega_{low}R$ as the velocity scale selects two of these parameters: the aspect ratio

$$\Gamma = H/R, \tag{2.1a}$$

and the Reynolds number

$$Re \equiv \Omega_{low}R^2/\nu. \tag{2.1b}$$

The third parameter can be taken to be the angular velocity ratio

$$s \equiv \Omega_{up}/\Omega_{low}. \tag{2.1c}$$

Note that consideration may be restricted to values $|s| \leqslant 1$, since values $|s| > 1$ can be mapped to $|s| \leqslant 1$ by inverting the upper and lower disks. We study the case of aspect ratio $\Gamma = 2$ and angular velocity ratio $s = -1$. That is, the height between the two disks is equal to the diameter of the disks, and the disks rotate at exactly equal and opposite angular velocities. The flow configuration is sketched in figure 1(*a*). The consequences of these choices will be discussed below. Throughout the paper, time is given in units of the rotation period, i.e. in units of $1/(2\pi\Omega_{low})$.

### 2.2. *Boundary conditions*

We denote by $(u, v, w)$ the components of the velocity $\boldsymbol{v}$ in cylindrical coordinates $(r, \theta, z)$. The boundary conditions on the cylinder walls are:

$$\boldsymbol{v} = 0 \qquad \text{on the stationary sidewall at } r = 1, \tag{2.2a}$$

$$\boldsymbol{v} = \mp r\boldsymbol{e}_\theta \quad \text{on the rotating disks at } z = \pm\tfrac{1}{2}\Gamma. \tag{2.2b}$$

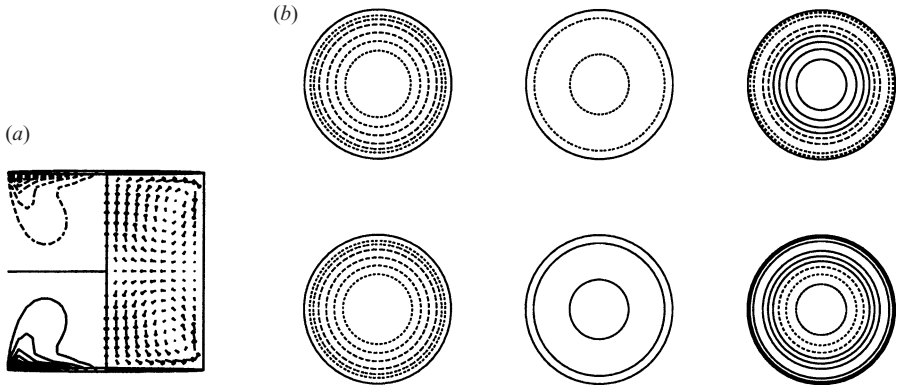


FIGURE 2. The basic state at $Re = 300$: ($a$) Contours of $v$ at $\theta = \pi$ (left) and vector field $(u, w)$ at $\theta = 0$ (right): positive (negative) values of $v$ are indicated by solid (dashed) curves. Note that $v$ changes sign under reflection in $z$. ($b$) Contours of radial (left), azimuthal (middle) and vertical (right) velocities at $z = \Gamma/4$ (top) and $z = -\Gamma/4$ (bottom). The views are seen from above. Note that $u$ is invariant under reflection in $z$, whereas $v$ and $w$ change signs. The maximum absolute values of $u$, $v$, and $w$ are 0.13, 1, and 0.11, respectively.

Boundary condition (2.2$a$) is, in fact, an additional specification of the flow under study. Rotating disk flows studied experimentally often specify a sidewall which instead rotates with one of the disks; other flows studied numerically may specify a sidewall whose angular velocity varies linearly with height between those of the upper and lower disks.

### 2.3. *Symmetries*

The basic flow consists of a dominant azimuthal shear layer produced by the counter-rotating lower and upper disks, as was first predicted by Batchelor (1951). There are also second-order recirculation zones due to Ekman pumping (figures 1 and 2$a$) in the neighbourhood of each disk. The two zones of the meridional flow meet at the mid-plane and converge to form an inwardly directed radial jet (figure 2$a$).

The configuration and basic state are invariant under rotations $S_{\theta_0}$ about the $z$-axis, i.e. they are axisymmetric. The case $s \equiv \Omega_{up}/\Omega_{low} = -1$, in which the angular velocities of the upper and lower disks are equal and opposite, is unique among the rotating disk configurations in possessing an additional symmetry of rotation of $\pi$ about any horizontal axis, in particular the $x$-axis, which we denote by $R_\pi$. This rotation is equivalent to the combined action of reflections in $\theta = 0$ and in $z = 0$. We define these symmetry operations by:

$$S_{\theta_0}\begin{pmatrix} u \\ v \\ w \end{pmatrix}(r, \theta, z) \equiv \begin{pmatrix} u \\ v \\ w \end{pmatrix}(r, \theta + \theta_0, z), \tag{2.3a}$$

$$R_\pi\begin{pmatrix} u \\ v \\ w \end{pmatrix}(r, \theta, z) \equiv \begin{pmatrix} u \\ -v \\ -w \end{pmatrix}(r, -\theta, -z). \tag{2.3b}$$

The crucial point is that $R_\pi$ does not commute with $S_{\theta_0}$ and hence, the group generated by these operators is isomorphic to $O(2)$, even though the rotation $R_\pi$ is not the usual reflection in $\theta$. These symmetries are illustrated in figure 2, which shows the basic flow at $Re = 300$.

The choice $s = 1$ of exactly co-rotating disks leads to the symmetry group $SO(2) \times Z_2$: the geometry and basic flow are invariant under rotations in $\theta$ and reflections in $z$. Since these operations commute, this group is not equivalent to $O(2)$. All other choices of $s$ lead to the symmetry group $SO(2)$.

### 2.4. *Normal form*

We now discuss the consequences of the choice $\Gamma = 2$ of aspect ratio. We have found that, in this case, the first instabilities to non-axisymmetric flow have azimuthal wavenumbers $m = 1$ and $m = 2$. Small azimuthal wavenumbers can be expected if the horizontal scale of the instability is approximately set by the vertical distance between the upper and lower boundaries which drive the instability (as is the case, for example, in Rayleigh–Bénard convection). (In § 6, we will argue that the vertical distance setting the scale of the instability is, in fact, the smaller thickness characterizing the equatorial shear layer.) We would expect a configuration of larger radius to favour instabilities with higher wavenumbers, since the circumference is then much larger than the height, and this is indeed the case, e.g. Marques & Lopez (2001), Marques *et al.* (2002), Lopez *et al.* (2002), Gelfgat *et al.* (2001).

Our calculations show that, for our aspect ratio $\Gamma = H/R = 2$, the basic state loses stability to non-axisymmetric modes $m = 1$ and $m = 2$ at Reynolds numbers which are fairly close: $Re_M = 349$ and $Re_P = 401$, respectively. Because of this, our hydrodynamic system is near the 1:2 resonance in the presence of $O(2)$ symmetry, a codimension-two bifurcation whose normal form was put forth and studied by Buzano & Russo (1987) and by Dangelmayr (1986) and investigated in detail by Armbruster, Guckenheimer & Holmes (1988) and by Proctor & Jones (1988).

Let $z_1 = x_1 + \mathrm{i}y_1$ and $z_2 = x_2 + \mathrm{i}y_2$ represent complex amplitudes of the $m = 1$ and $m = 2$ modes. Here and throughout the paper, the use of subscripts indicates that $x_j, y_j, z_j$ refer to mode amplitudes in a normal form, rather than to coordinate directions. The symmetry operations $S_\theta$ and $R_\pi$ are represented in the usual way by:

$$S_\theta(z_1, z_2) = (\mathrm{e}^{\mathrm{i}\theta} z_1, \mathrm{e}^{2\mathrm{i}\theta} z_2), \tag{2.4a}$$

$$R_\pi(z_1, z_2) = (\overline{z_1}, \overline{z_2}). \tag{2.4b}$$

The four-dimensional system of evolution equations for $(z_1, z_2)$ is formulated to contain all terms up to cubic order which are compatible with (2.4), i.e. equivariant under the group generated by (2.4*a*) and (2.4*b*) (Golubitsky, Stewart & Schaeffer 1988; Crawford & Knobloch 1991):

$$\dot{z}_1 = \overline{z_1} z_2 + z_1(\mu_1 + e_{11}|z_1|^2 + e_{12}|z_2|^2), \tag{2.5a}$$

$$\dot{z}_2 = \pm z_1^2 + z_2(\mu_2 + e_{21}|z_1|^2 + e_{22}|z_2|^2), \tag{2.5b}$$

where $\mu_j$ and $e_{jk}$ are real parameters.

Steady solutions of (2.5) are the trivial solution $z_1 = z_2 = 0$, the *pure modes P* satisfying $z_1 = 0, z_2 \neq 0$, and the *mixed modes M* satisfying $z_1 \neq 0, z_2 \neq 0$. As can be seen from (2.5), there are no steady solutions satisfying $z_1 \neq 0, z_2 = 0$. It is for this reason that states $M$ are termed mixed modes. We see from (2.4*b*) that the solutions which are invariant under $R_\pi$ are those with $y_1 = y_2 = 0$.

Among all cases of $m : n$ mode interaction, the $1:2$ resonance is distinguished for the following reason. Mode interactions between competing instabilities typically occur between neighbouring wavenumbers, $m$ and $m + 1$. The branches arising at these bifurcations contain harmonics of the fundamental wavenumbers. The pair

$m : m+1 = 1:2$ is the only one in which one wavenumber is the first (and hence strongest) harmonic of the other: i.e. $m+1 = 2m$. The quadratic terms in (2.5) attest to the importance of the $1:2$ mode interaction. We note that, except for the cases $1:2$ and $1:3$, all of the equations describing mode interactions between wavenumbers $m$ and $n$ are identical when truncated to cubic order, and consist of equations (2.5) with the quadratic terms omitted. (The equations describing the $1:3$ case contain two types of cubic term.) See Dangelmayr (1986) and Golubitsky *et al.* (1988) for a derivation.

Travelling-wave solutions are best described by transforming the normal form amplitudes to polar coordinates via $z_j = r_j \exp \mathrm{i}\theta_j$. Again, the use of subscripts on $r_j, \theta_j$ indicates that these are normal form amplitudes rather than coordinate directions. Defining $\phi \equiv 2\theta_1 - \theta_2$, the system (2.5) can be rewritten as the three-dimensional system:

$$\dot{r}_1 = r_1 r_2 \cos\phi + r_1(\mu_1 + e_{11} r_1^2 + e_{12} r_2^2), \tag{2.6a}$$

$$\dot{r}_2 = \pm r_1^2 \cos\phi + r_2(\mu_2 + e_{21} r_1^2 + e_{22} r_2^2), \tag{2.6b}$$

$$\dot{\phi} = -\left(2r_2 \pm r_1^2/r_2\right) \sin\phi. \tag{2.6c}$$

Steady solutions of (2.5) correspond to fixed points of (2.6) with $\phi = 0$ or $\pi$. Travelling-wave solutions of (2.5) are fixed points of (2.6) with $\phi \neq 0,\ \pi$ in which $\phi$ remains constant but $\theta_1$ and $\theta_2$ vary linearly with time such that $2\dot{\theta}_1 = \dot{\theta}_2$ and $2r_2^2 = r_1^2$.

Armbruster *et al.* (1988) conducted an exhaustive analysis of the behavior of the normal form (2.5), analysing the dependence of the possible solutions on the values of $\mu_j, e_{jk}$ and, crucially, on the sign in (2.5*b*) or (2.6*b*)–(2.6*c*). In particular, for the negative sign, they showed that there exists a rich variety of distinct dynamical states, including travelling waves, modulated travelling waves and, most remarkably, heteroclinic cycles connecting two pure mode states which persist over a range of parameter values. The parameters $e_{jk}$ are considered as fixed and $\mu_1$ and $\mu_2$ control instability of the trivial state to mixed and pure modes; $\mu_1 = \mu_2 = 0$ is the codimension-two point at which both instabilities occur simultaneously. A similar analysis was carried out simultaneously by Proctor & Jones (1988), who derived the normal form (2.5) as amplitude equations for convection in two superimposed fluid layers, heated from below and separated by a conducting plate. The exotic and ubiquitous nature of the $1:2$ resonance has continued to inspire many other studies involving further mathematical analysis (Kevrekidis, Nicolaenko & Scovel 1990; Porter & Knobloch 2001; Chossat 2001) and applications to physical phenomena such as turbulent boundary layers (Aubry *et al.* (1988)) and thermal convection (Cox 1996; Mercader, Prat & Knobloch 2001).

Our study of the von Kármán flow leaves no doubt that it is remarkably well described by the normal form (2.5) in the negative sign case. The parameters $\mu_1$ and $\mu_2$ can be considered to be control parameters embodying some combination of $Re$ and $\Gamma$. Our study, with $\Gamma$ fixed and $Re$ varied, corresponds to traversing a path in the $\mu_1, \mu_2$ parameter space. We find mixed modes, pure modes, travelling waves, modulated travelling waves, and heteroclinic cycles linking two different pure mode states. We have studied this sequence of steady and time-dependent states and the transitions between them by means of direct computations of the fully nonlinear three-dimensional Navier–Stokes equations. We have been able to extract additional dynamical information by employing linearization and symmetry restrictions. These numerical tools are described in the next section.

## 3. Numerical techniques

### 3.1. *Nonlinear non-axisymmetric evolution*

Our main computational tool is a code which carries out time integration of the nonlinear non-axisymmetric Navier–Stokes equations.

$$\nabla \cdot \boldsymbol{v} = 0, \tag{3.1a}$$

$$\frac{\partial \boldsymbol{v}}{\partial t} + (\boldsymbol{v} \cdot \nabla)\boldsymbol{v} = -\nabla p - \frac{1}{Re}\nabla \times \nabla \times \boldsymbol{v}. \tag{3.1b}$$

(The diffusion terms are written in curl(curl) form, which allows for the use of the mimetic curl operator which will be discussed below.) In this section, we outline only the main features of our code. More details can be found in Barbosa & Daube (2001).

#### 3.1.1. *Spatial discretization*

We expand the velocity components and pressure in truncated Fourier series over $N_\theta$ modes, the coefficients of which are discretized in the $(r, z)$-planes. The main difficulty associated with the use of cylindrical coordinates is the treatment of the $r = 0$ axis. This is dealt with by using *mimetic* finite difference operators (Hyman & Shashkov 1997), meaning that they satisfy the discrete analogues of the usual vector analysis relations. The main ingredients of this discretization are:

A staggered MAC uniform grid is used in the $(r, z)$-plane. Two kinds of cells are used, one for cells far from the axis, the other for cells having an edge $r = 0$. Both are displayed in figure 3.

The first-order discrete operators $\mathrm{div}_h$ and $\mathrm{curl}_h$ are defined by means of a discrete quadrature by the trapezoïdal rule of Gauss' theorem over a cell and of Stokes' theorem along suitable loops.

Discrete counterparts of the standard inner products of the continuum case are defined on the sets of discrete scalar and vector functions.

The discrete gradient operator is defined as the negative adjoint of the discrete divergence operator with respect to these discrete inner products.

The nonlinear terms are discretized in such a way as to be energetically neutral in the sense of the discrete inner product.

The discrete vector diffusion operator $\nabla_h^2$ is defined as two applications of the discrete curl $(-\nabla_h \times \nabla_h \times)$, using the fact that the discrete divergence vanishes.

Fast direct solvers based upon a partial diagonalization technique (Haidvogel & Zang 1979) in the $z$-direction are used to solve the resulting discrete systems.

#### 3.1.2. *Temporal discretization*

We write the Navier–Stokes equations schematically as

$$\frac{\partial \boldsymbol{v}}{\partial t} = \boldsymbol{L} + \boldsymbol{N}, \tag{3.2}$$

where $\boldsymbol{L}$ represents the linear viscous terms and $\boldsymbol{N}$ the nonlinear terms. Equation (3.2) is approximated at timestep $n + 1$ by the following second-order time-stepping scheme (Vanel, Peyret & Bontoux 1986):

$$\frac{3\boldsymbol{v}^{n+1} - 4\boldsymbol{v}^n + \boldsymbol{v}^{n-1}}{2\Delta t} = \boldsymbol{L}^{n+1} + 2\boldsymbol{N}^n - \boldsymbol{N}^{n-1} + O(\Delta t^2) \tag{3.3}$$

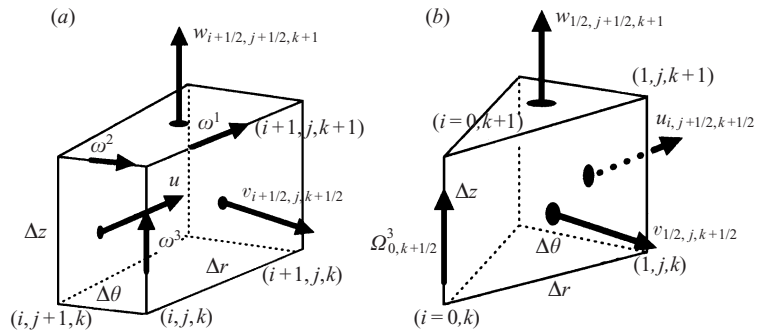


FIGURE 3. The MAC grid: the regular cells, shown in (*a*), are parallelipipedic while the axis cells, shown in (*b*), are triangular. Velocity components are defined at the middle of the faces while the vorticity components are defined at the middle of the sides.

Equation (3.3) yields a Helmholtz problem for $(\boldsymbol{v}^{n+1}, p^{n+1})$:

$$\left(\frac{3Re}{2\Delta t}\,\boldsymbol{I} + \nabla\times\nabla\times\right)\boldsymbol{v}^{n+1} + \nabla p^{n+1} = \boldsymbol{S}^{n,n-1}. \tag{3.4}$$

The source terms $\boldsymbol{S}^{n,n-1}$ contain all the quantities which are evaluated at previous time steps.

### 3.1.3. *Velocity–pressure coupling*

The usual difficulty which arises in numerical integration of the incompressible Navier–Stokes equations lies in the velocity–pressure coupling through the vanishing divergence of the velocity. This is handled by means of an incremental projection method (Goda 1979):

Prediction step: Find a provisional velocity field $\boldsymbol{v}^*$ which satisfies:

$$\left(\frac{3Re}{2\Delta t}\,\boldsymbol{I} + \nabla\times\nabla\times\right)\boldsymbol{v}^* = -\nabla p^n + \boldsymbol{S}^{n,n-1},$$

with the no-slip boundary conditions.

Projection step: Project $\boldsymbol{v}^*$ on the space of divergence-free vector fields. This is achieved by setting $\boldsymbol{v}^{n+1} = \boldsymbol{v}^* + \nabla\phi$. The auxiliary function $\phi$ is computed by solving a Poisson equation with Neumann boundary conditions:

$$-\nabla\cdot(\nabla\phi) = \nabla\cdot\boldsymbol{v}^*,$$
$$\frac{\partial\phi}{\partial n} = 0 \quad \text{on the boundary,}$$

and the pressure $p^{n+1}$ is classically recovered as:

$$p^{n+1} = p^n - \left(\frac{3\phi}{2\Delta t} + \frac{\nabla\cdot\boldsymbol{v}^*}{Re}\right).$$

## 3.2. *Steady states and linear stability*

Our goal is to carry out a full bifurcation analysis of the von Kármán flow for our parameter range. To do this, we have used several computational techniques in addition to that described in § 3.1.

3.2.1. *Axisymmetric steady states*

The axisymmetric steady states are not computed using the code described in § 3.1. Instead, the equations are written in the streamfunction–vorticity formulation and the influence matrix technique is used to satisfy the no-slip boundary conditions. The steady states can then be calculated via Newton's method with Stokes preconditioning, as described by Mamun & Tuckerman (1995). The steady states obtained in this way are more accurate than those that would be obtained by time-integration. GMRES (Saad & Schultz 1986) is used to solve the linear system required by each Newton iteration. GMRES is an example of a matrix-free method, requiring only computation of the action of the linearized operator on a vector. A matrix–vector multiplication is equivalent to taking one timestep of the linearized Navier–Stokes equations; see Mamun & Tuckerman (1995) for more details.

3.2.2. *Non-axisymmetric steady states*

Our non-axisymmetric steady states are obtained by time-integration of the nonlinear non-axisymmetric Navier–Stokes equations as described in § 3.1. Normally, only stable steady states would be accessible to time-integration. However, most of our bifurcations are symmetry-breaking. We can therefore calculate unstable steady states by imposing a symmetry. We have done this in particular to calculate the branch of pure mode states which is the second to bifurcate from the axisymmetric branch. The Fourier series for the pure mode states contain only even azimuthal wavenumbers. Such flows constitute an invariant subspace for the Navier–Stokes equations, corresponding to the fact that $z_1 = 0$ is preserved in the normal form (2.5), and the pure mode states are stable when integration is carried out in this subspace. (In contrast, the mixed mode states contain both even and odd wavenumbers.) Another branch of unstable steady states which we have been able to calculate is the mixed-mode branch after it becomes unstable to travelling waves. Since the eigenvector responsible for this bifurcation is antisymmetric with respect to our reflection operator $R_\pi$, the mixed-mode branch remains stable when integration is carried out in the subspace of flows symmetric under $R_\pi$.

3.2.3. *Linear stability*

Linear stability analysis of axisymmetric and non-axisymmetric steady states is carried out by temporal integration of the Navier–Stokes equation linearized about the steady state. That is, the governing equations (3.1) are modified to read:

$$\nabla \cdot \boldsymbol{v} = 0, \tag{3.5a}$$

$$\frac{\partial \boldsymbol{v}}{\partial t} + (\boldsymbol{V} \cdot \nabla)\boldsymbol{v} + (\boldsymbol{v} \cdot \nabla)\boldsymbol{V} = -\nabla p - \frac{1}{Re}\nabla \times \nabla \times \boldsymbol{v}, \tag{3.5b}$$

where $\boldsymbol{V}$ is a previously computed steady state. This is equivalent to carrying out the power method on the approximate exponential of the Jacobian operator (Mamun & Tuckerman 1995). The power method computes the dominant eigenvalue (of largest magnitude) of the approximate exponential operator, which is the leading eigenvalue (of largest real part) of the Jacobian. The leading eigenvalue is the unstable or least stable eigenvalue and is responsible for the bifurcations undergone by the steady state. Long-time integration yields the leading eigenvector and its growth rate, the leading eigenvalue.

In general, the power method computes only a single leading eigenvalue. However, for an axisymmetric state, eigenvectors corresponding to different azimuthal wavenumbers $m$ belong to different invariant subspaces which are decoupled from

one another. Therefore integration of the linearized equations from an arbitrary initial condition is equivalent to carrying out $N_\theta$ integrations in parallel, one for each Fourier component $m$. The leading eigenvector corresponding to each $m$ is merely the corresponding Fourier component of the field resulting from long-time integration, and the leading eigenvalue corresponding to $m$ is its growth rate.

Linearized evolution about non-axisymmetric steady states couples different Fourier components; the eigenvectors are superpositions of Fourier modes. However, for steady states possessing other symmetries, there exist other subspaces which are invariant under linearized evolution; the eigenvectors necessarily belong to these invariant subspaces. In particular, for a steady state which is symmetric under $R_\pi$, all eigenvectors are either symmetric or antisymmetric. In terms of the normal form (2.5), this corresponds to the fact that the eigenvectors of steady states of the form $(x_1, y_1, x_2, y_2) = (x_1, 0, x_2, 0)$ are either of the form $(x_1, 0, x_2, 0)$ or of the form $(0, y_1, 0, y_2)$. The symmetric eigenvectors can be extracted from the result of linearized evolution by computing the symmetric part $\{(\boldsymbol{I}+R_\pi)/2\}\ (u, v, w)$ and the antisymmetric eigenvectors by computing $\{(\boldsymbol{I} - R_\pi)/2\}\ (u, v, w)$. Thus, two leading eigenvalues can be extracted from the power method.

Similarly, we can make use of the symmetry of the pure mode states, whose Fourier series contain only even wavenumbers. Flows containing only even or only odd Fourier components are invariant under linearized evolution about the pure mode states. The eigenvectors thus belong to these invariant subspaces. Even and odd eigenvectors are extracted after long-time integration by separating the even and odd Fourier components. Since the phase of the pure mode states can in addition be chosen so as to make them symmetric under $R_\pi$, a total of four leading eigenvectors can be extracted from a single long-time integration corresponding to the four possible combinations of even and odd, reflection-symmetric and reflection-antisymmetric. These correspond to the four components of the normal form (2.5). It is not possible to do this for the mixed modes, since their eigenvectors are superpositions of Fourier modes with both even and odd wavenumbers. In order to calculate four leading eigenvectors of the mixed modes, we instead used ARPACK (Lehoucq, Sorensen & Yang 1998) or our own implementation of the Arnoldi method (Mamun & Tuckerman 1995).

### 3.3. *Code validation and resolution*

Our code was tested by comparing our linearized computations with the thresholds computed by Gelfgat *et al.* (2001) for the case $\Gamma = 1$ and $s = 0$, for which the first instability is to an $m = 2$ mode. We give some partial results which may be found in Barbosa & Daube (2001). Figure 4 shows the variation of the threshold with the resolution $N_r = N_z = N$ and $N_\theta = 32$. A parabolic fit gives $Re_{m=2} = 2473$, to be compared with 2471 found by Gelfgat *et al.* (2001) using spectral methods. The threshold for $N = 101$ is 2447, differing by 1% from the spectral result.

In the results reported in this paper, all computations are performed with $N_r = 101$, $N_\theta = 32$, $N_z = 201$ unless otherwise specified and $\Gamma = 2$ and $s = -1$. This resolution was checked to be sufficient for the Reynolds number range under study. The timestep is $\Delta t = 10^{-2}$ nondimensional time units and a typical run of 400 disk rotations takes 3 hours on a NEC-SX5 computer.

## 4. Primary bifurcations

We begin by determining the critical Reynolds numbers at which the basic axisymmetric state loses stability. The branch of steady states with $m = 1$ is the first

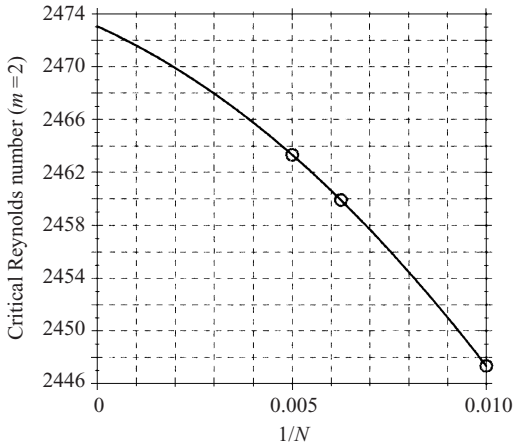


FIGURE 4. Critical Reynolds number for $\Gamma = 1$, $s = 0$ and azimuthal wavenumber $m = 2$. A parabolic fit gives $Re_{m=2} = 2473$, in excellent agreement with Gelfgat *et al.* (2001).

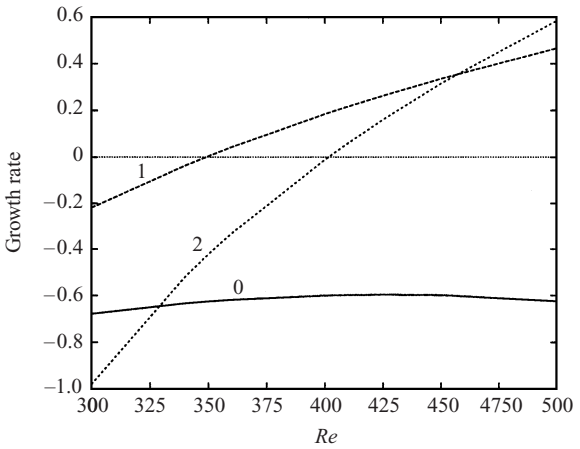


FIGURE 5. Growth rate of azimuthal energy components 0, 1, 2 as a function of $Re$. The crossing of the Reynolds number axis defines linear thresholds $Re_M = 349.0$ and $Re_P = 401.5$.

to bifurcate from the basic state as $Re$ increases, followed by the pure modes $m = 2$. The thresholds are determined by plotting the growth rate of each azimuthal energy component as a function of $Re$ (figure 5). Throughout the paper, we report thresholds to one decimal digit in the Reynolds number the first time they are mentioned and also whenever increased precision is significant. Otherwise, we report thresholds as integer values of the Reynolds number.

The first bifurcation occurs at $Re_M = 349.0$ and the second at $Re_P = 401.5 \simeq 401$. Figure 6 shows vertical velocity contours of the $m = 1$ eigenvector at $Re = 355$ and the $m = 2$ eigenvector at $Re = 410$, just above the bifurcation thresholds. Both of these eigenvectors are invariant under the reflection symmetry $R_\pi$. This can be easily checked at $z = 0$ where the negative contours for $0 < \theta < \pi$ correspond to the positive contours for $\pi < \theta < 2\pi$. The $w = 0$ contour in this plane is straight and horizontal. The action of $R_\pi$ relating contours at $z = \Gamma/6$ and $z = -\Gamma/6$ is more complicated: take a feature in the $\Gamma/6$ plane, flip it (reflect in $\theta$), change its sign, and find it in the $-\Gamma/6$ plane.

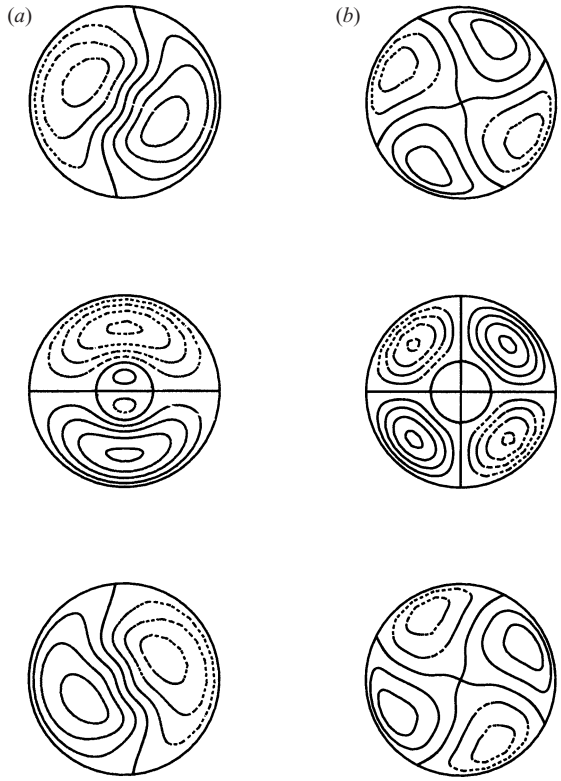


FIGURE 6. Vertical velocity contours at $z = \Gamma/6$ (top), $z = 0$ (middle), and $z = -\Gamma/6$ (bottom) of the eigenvectors of the unstable basic state: (*a*) $m = 1$ at $Re = 355$, (*b*) $m = 2$ at $Re = 410$. These non-axisymmetric eigenvectors retain $R_\pi$ symmetry: at $z = 0$, the negative (dashed) contours for $0 < \theta < \pi$ correspond to the positive (solid) contours for $\pi < \theta < 2\pi$. The action of $R_\pi$ between $\Gamma/6$ and $-\Gamma/6$ is as follows: take a feature in the $\Gamma/6$-plane, flip it (reflect in $\theta$), change its sign and find it in the $-\Gamma/6$-plane.

The bifurcations are circle pitchforks, involving a two-dimensional eigenspace and creating a 'circle' of steady states parametrized by angular phase $\theta_0$. In addition, standard analysis of the circle pitchfork under $O(2)$ symmetry, and, more generally the equivariant branching lemma (Golubitsky *et al.* 1988) dictate that the nonlinear states are also symmetric under $R_\pi$. These features are a consequence of the exact counter-rotation of the top and bottom disks ($s = -1$). For any case with $|s| \neq 1$, the symmetry group would be $SO(2)$ and a bifurcation breaking azimuthal symmetry would generically lead to rotating waves, cf. Crawford & Knobloch (1991).

Both bifurcations are supercritical, as can be determined by temporally integrating the system near the threshold from the basic state (Henderson & Barkley 1996). Figure 7 shows that the linear phase for the transition to the mixed mode at $Re = 355$ (or to the pure mode at $Re = 405$) extends to $t \simeq 300$ (or to $t \simeq 400$) and that, subsequently, when nonlinear effects come into play, the slope decreases. The $w$ velocity shown in figure 7 can be thought of as representing the amplitude $a$ of the bifurcating mode in a normal-form model $\dot{a} = \mu a + \alpha a^3$. In both cases the fact that the slope decreases after the linear phase of the evolution shows that $\alpha$ is negative, thus proving that the pitchfork bifurcation is supercritical.

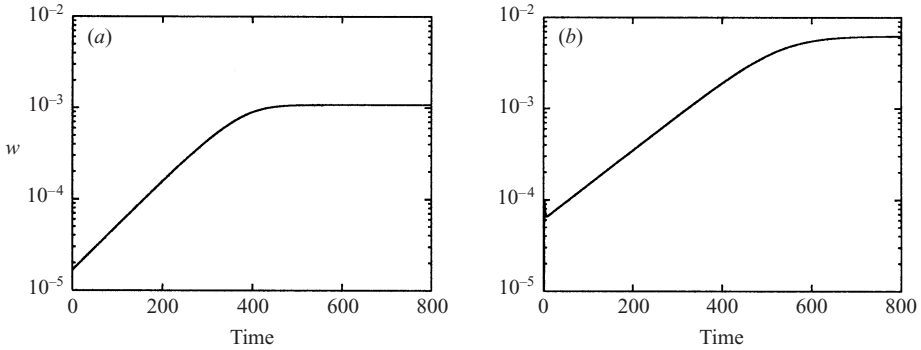


FIGURE 7. Evolution of $\log(w(1/2,0,0))$ from the basic state. Initial phase of exponential growth is followed by a nonlinear phase of slower growth, indicating a supercritical bifurcation in both cases. (*a*) Transition to mixed mode at $Re = 355$. (*b*) Transition to pure mode at $Re = 405$.

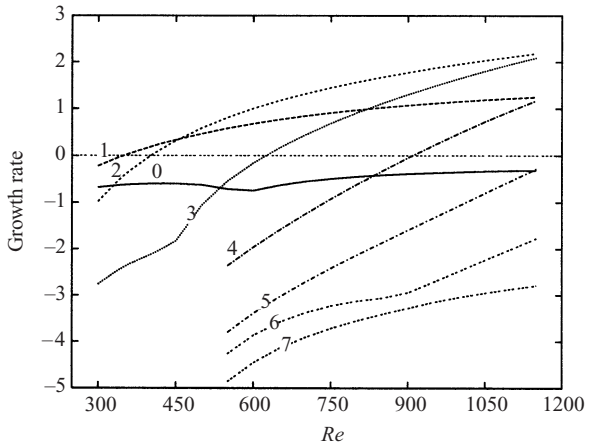


FIGURE 8. Growth rate of azimuthal energy components $0 \leqslant m \leqslant 7$ as a function of $Re$. Note that, in the range $0 \leqslant Re \leqslant 500$, only $m = 1$ and $m = 2$ modes bifurcate.

Thresholds for $m = 1, 2$ differ by less than 1% for two resolutions $(N_r, N_z) = (101, 201)$ and $(N_r, N_z) = (161, 321)$.

## 5. Sequence of steady and time-dependent states

As a guide to our observations, we begin by showing in figure 9 a schematic view of the sequence of steady and time-dependent states observed. Stable branches are indicated by solid curves and unstable branches by dashed curves. We will describe in detail each of the states encountered, i.e. mixed modes, travelling and modulated waves, pure modes, and finally, heteroclinic cycles. This ordering is essentially (but not entirely) consistent with the order in Reynolds number in which these states are observed.

### 5.1. *Mixed modes*

The branch of mixed modes $M$ bifurcates from the basic state at $Re_M = 349$. It loses stability at $Re_{TW} = 411.6 \simeq 412$ and ceases to exist at $Re_{MP} = 418.4 \simeq 418$ via bifurcations which we will discuss in later sections. The symmetries of the mixed

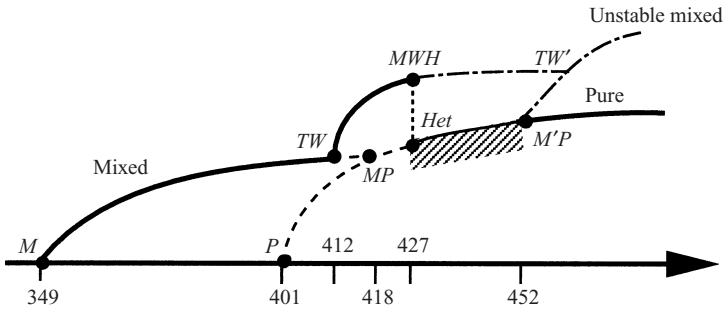


FIGURE 9. Theoretical bifurcation diagram as a function of $Re$. Stable solutions are indicated by solid lines, unstable ones by dashed lines and shaded lines denote attracting heteroclinic cycles. Dot-dashed lines indicate branches which we have not computed. Thresholds are indicated by dots: $Re_M = 349$, $Re_P \simeq 401$, $Re_{TW} \simeq 412$, $Re_{MP} \simeq 418$, $Re_{MWH} = 427.3$, $Re_{Het} = 427.4$, $Re_{M'P} \simeq 452$.

modes $M$ can be observed in figure 10$a$, showing contours of the vertical velocity $w$ at $z = -\Gamma/6$, 0, and $\Gamma/6$. Contours of $w$ in the $z = 0$ plane are especially useful in depicting our nonaxisymmetric flows, since $w = 0$ in this plane for the basic axisymmetric flow. The mixed mode retains the $R_\pi$ symmetry.

Physically, the mixed mode state $M$ can be viewed as the result of the first instability of the equatorial shear layer produced by the counter-rotating disks. Azimuthal disturbances saturate and engender a 'vortex monopole' shown in figure 10$(b, d)$. The vortex centre is an elliptic point located near $r = 1$, $\theta = \pi$, $z = 0$; the corresponding hyperbolic point is located diametrically opposite at $r = 1$, $\theta = 0$, $z = 0$ (see figure 10$d$). The vector field $(u, w)$ and contours of $v$ are symmetric about the mid-plane in the meridional planes $\theta = 0, \pi$ (figure 10$c$, top) but deformed in the meridional planes perpendicular to the vortex $\theta = \pi/2, 3\pi/2$ (figure 10$c$, bottom). The radially inward jet associated with the recirculation zones of the meridional plane (figure 10$c$) acquires a wavy shape and intensity. Contours of the radial velocity $u$ resemble those of the radial vorticity $\omega_r$ in figure 10$(d)$, meaning that the inflow jet has a maximum at the vortex centre.

The mixed mode branch is destroyed via a pitchfork bifurcation onto the pure mode branch at $Re_{MP} = 418$, in accordance with the analysis of Armbruster *et al.* (1988) and of Proctor & Jones (1988). Thus, the mixed mode branch evolves from an entirely $m = 1$ harmonic content at $Re_M = 349$ to an entirely even $m = 2, 4, \ldots$ harmonic content at $Re_{MP} = 418$, justifying the nomenclature of mixed mode.

The bifurcations undergone by the mixed mode state are accompanied by changes of sign of the leading eigenvalues. Figure 11 shows the leading eigenvalues of the mixed mode state over the range of its existence $Re_M = 349 \leqslant Re \leqslant Re_{MP} = 418.4$, preceded by those of the basic state for $Re \leqslant Re_M = 349$. These meet continuously (but not smoothly) at $Re_M$ because the mixed mode and basic states are identical at the threshold of the mixed mode branch.

For the basic state, an axis of symmetry has not been selected and the notion of reflection symmetry is meaningless. Eigenvectors with $m \neq 0$ instead are grouped into two-dimensional eigenspaces. Thus, for the basic branch, eigenvalue $\lambda_1$, associated with Fourier mode $m = 1$ and eigenvalue $\lambda_2$, associated with $m = 2$, each correspond to two degenerate eigenvectors. The degeneracy is lifted when $\lambda_1$ crosses zero at $Re_M = 349$: any mixed mode state has a symmetry axis and its eigenvectors can be classified as either symmetric or antisymmetric, each associated with different eigenvalues (which we also term symmetric or antisymmetric). However, the Fourier modes cease

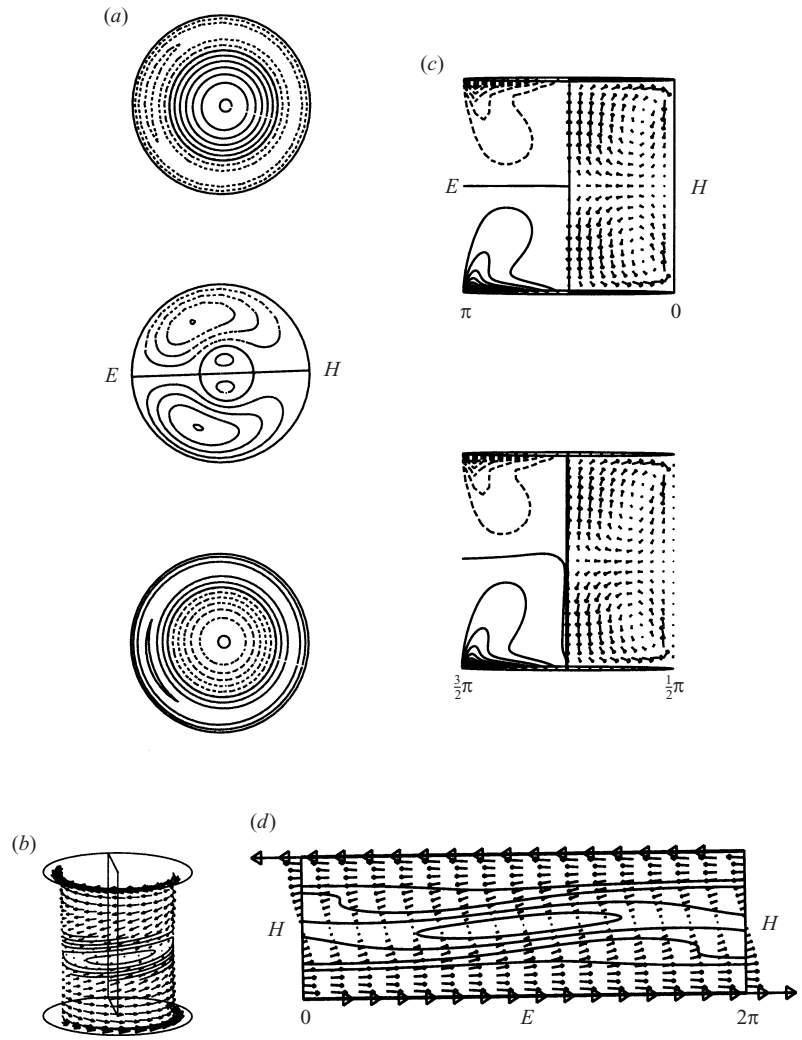


FIGURE 10. The mixed mode state at $Re = 355$, near the bifurcation at $Re_M = 349$. (*a*) Vertical velocity contours at $z = \Gamma/6$ (top), $z = 0$ (middle), and $z = -\Gamma/6$ (bottom). The views are seen from above. (*b*) Vector field $(v, w)$ and contours of $\omega_r$ showing a 'vortex monopole' at $r = 0.75$ and $\theta = \pi$. (*c*) Vector field $(u, w)$ at $\theta = 0$ and contours of $v$ at $\theta = \pi$ through the vortex (top) and at $\theta = \pi/2,\ 3\pi/2$ perpendicularly to the vortex (bottom). (*d*) Unfolded vector field $(v, w)$ and contours of $\omega_r$ at $r = 0.75$. The vortex is centred on the elliptic point near $\theta = \pi$, $z = 0$ and diametrically opposite from the hyperbolic point near $\theta = 0$, $z = 0$.

to be separate: each eigenvector about a mixed mode contains components of all wavenumbers.

The eigenvalues emanating from zero at $Re_M$ are standard features of any circle pitchfork bifurcation. The symmetric eigenvector resembles the difference between the mixed mode and the base flow; its eigenvalue becomes negative with increasing $Re$, as it is stabilized by the circle pitchfork. The antisymmetric eigenvector corresponding to rotation in $\theta$ is a neutral mode whose eigenvalue remains zero.

The eigenvalue $\lambda_2$ also splits into symmetric and antisymmetric parts. Figure 11 shows that the symmetric eigenvalue joins with the other leading symmetric eigenvalue at $Re \approx 365$ to form a complex conjugate pair. (This behaviour is also found in the

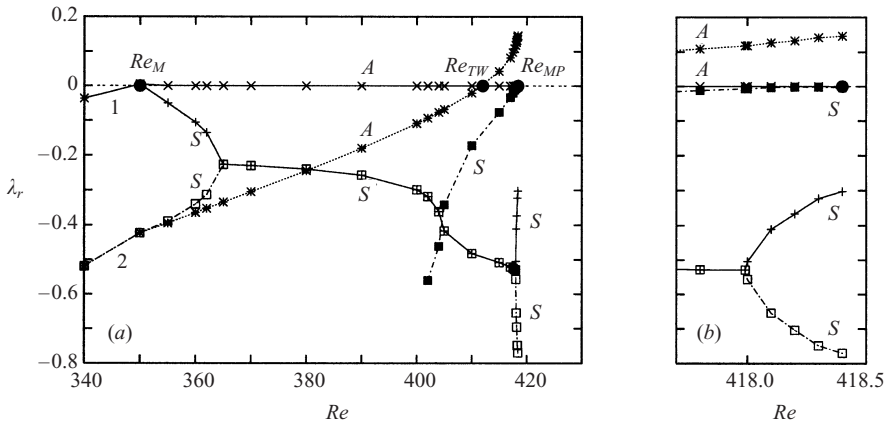


FIGURE 11. (*a*)The four/five most dangerous eigenvalues as functions of $Re$ about the basic state for $Re \leqslant Re_M = 349$ and about the mixed mode state for $Re_M = 349 \leqslant Re \leqslant Re_{MP} = 418.4$. For the basic state, the symbols 1 and 2 refer to the two-dimensional eigenspace corresponding to $m = 1$ and $m = 2$, respectively. For the mixed mode state, eigenvectors are classified as symmetric ($S$) or antisymmetric ($A$) under $R_\pi$. The mixed mode branch is created at a circle pitchfork bifurcation at $Re_M$, where the $m = 1$ eigenvalue splits into bifurcating ($S$, +) and marginal ($A$, ×) modes. Of the two branches resulting from the $m = 2$ eigenvalue, one ($S$, □) merges with the other symmetric eigenvalue to become a complex conjugate pair at $Re \approx 365$; their real part is shown. The mixed mode branch loses stability when the other eigenvalue ($A$; *) crosses zero at $Re_{TW} = 412$, and is destroyed when a fifth eigenvalue ($S$; ■) crosses zero at $Re_{MP} = 418.4$. The fifth eigenvalue branch does not cross any of the others, although it coincides with the real part of the complex conjugate branch at $Re = 405$. (*b*) An enlargement of the five eigenvalues near $Re_{MP}$, showing that the complex conjugate pair splits into a real pair over the range $418 \leqslant Re \leqslant 418.4$.

normal form (2.5) for some parameter values.) The antisymmetric eigenvalue continues to increase with $Re$ until it crosses zero at $Re_{TW} = 412$ at a drift pitchfork bifurcation discussed in the next section.

Another eigenvalue, this one symmetric, necessarily traverses zero at $Re_{MP} = 418.4$. The unexpected feature of figure 11 is that this eigenvalue is not the continuation of any of the four leading eigenvalues at $Re_M$. Instead, at $Re \approx 405$, a fifth eigenvalue crosses the real part of the complex conjugate pair, continues to increase, and is finally responsible for the pitchfork bifurcation which destroys the mixed mode branch at $Re_{MP}$. This sequence of events is confirmed by the enlargement in figure 11, establishing that the symmetric eigenvalues involved in the generation of the mixed and pure modes remain negative at $Re_{MP}$. This is discussed further in § 5.5.

### 5.2. *Travelling waves and modulated waves*

The mixed mode branch loses stability at $Re_{TW} = 411.6 \approx 412$, giving rise to a pair of travelling waves (TW), one rotating clockwise and the other counterclockwise. A clockwise rotating wave is represented in figure 12(*a*). It can be checked that the $R_\pi$ symmetry has been broken because there is no straight zero value contour in the $z = 0$ plane of figure 12(*a*). Because the drift pitchfork breaks reflection symmetry, we have been able to follow the unstable branch of mixed mode states above $Re_{TW}$ by imposing the $R_\pi$ symmetry at each timestep, as explained in § 3.2.3. For example, the corresponding unstable mixed mode state at $Re = 415$ is represented in figure 12(*b*). We can compute the linear eigenvectors of the unstable mixed mode states which are responsible for the TW instability in this Reynolds number range. The eigenvector responsible for the TW state at $Re = 415$ appears in figure 12(*c*). Its antisymmetry

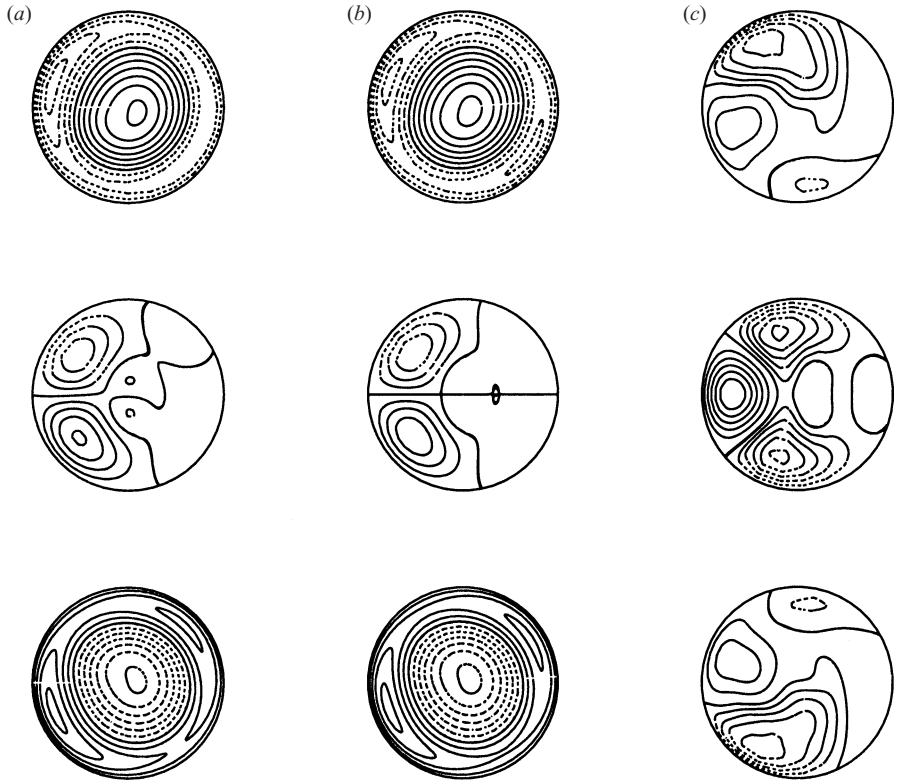


FIGURE 12. Vertical velocity contours at $z = \Gamma/6$ (top), 0 (middle), $-\Gamma/6$ (bottom) at $Re = 415$ for ($a$) the TW state, ($b$) the (unstable) M mode state and ($c$) the antisymmetric eigenvector responsible for the TW instability. In (a) the $R_\pi$ symmetry has been broken because there is no straight $w = 0$ contour in the $z = 0$ plane. In ($b$), the unstable $M$ mode is symmetric. In ($c$), the antisymmetry is manifested by the fact that $w$ does not change sign when it is flipped between $z = \Gamma/6$ and $z = -\Gamma/6$.

is manifested by the fact that $w$ does not change sign under $R_\pi$, meaning that $w(r, \theta, z) = w(r, -\theta, -z)$.

We have computed the nonlinear rotating wave states for several Reynolds numbers. Figure 13 shows that the inverse of the period is proportional to $\sqrt{Re - Re_{TW}}$, with the critical Reynolds number for the drift bifurcation $Re_{TW} = 411.6$ determined by extrapolation. This relation confirms that the bifurcation is a drift pitchfork and establishes that it is supercritical. The energy of each Fourier component of the travelling waves is constant because the pattern is steady in the frame rotating with the precession wavespeed.

The TW lose stability at a Hopf bifurcation whose threshold $Re_{MWH} = 427.3$ is determined by fitting the initial temporal evolution of the energy to the function

$$E(t) = \exp(\sigma t)\cos(\omega(t - t_0)). \tag{5.1}$$

Figure 14 shows the frequency $\omega$ and the growth rate $\sigma$ as a function of $Re$. This Hopf bifurcation should produce modulated waves (MW) at $Re_{MWH} = 427.3$. In our case, these occur in a very reduced range of Reynolds numbers. Figure 15 shows the stable oscillations in energy typical of modulated waves at $Re = 427.35$. Figure 14 shows that the modulation frequency is 4–5 times that of the underlying travelling

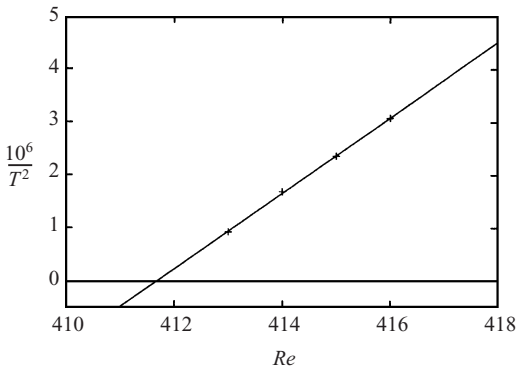


FIGURE 13. Square of the rotating wave frequency as a function of $Re$. A straight-line fit indicates a drift pitchfork at $Re_{TW} = 411.6$ determined by extrapolation.

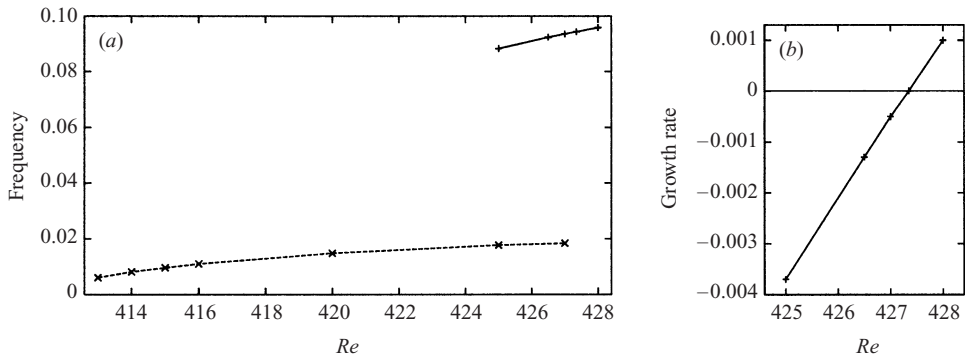


FIGURE 14. Hopf bifurcation from travelling waves to modulated travelling waves. ($a$) Frequency $\omega$ of energy $E(t)$ associated with Hopf bifurcation (solid line) and of underlying travelling waves (dashed line). The modulation frequency is about five times that of the travelling waves. ($b$) Growth rate $\sigma$ of energy. The crossing of the Reynolds number axis determines $Re_{MWH} = 427.3$ for Hopf bifurcation from travelling waves.

waves. In the velocity signal of figure 15, the modulation is barely visible as a slight variation in shape from one oscillation to the next.

Since our methods do not permit us to follow the TW branch past $Re_{MWH}$, we cannot be sure of its eventual fate. The simplest outcome, illustrated in the analysis of Armbruster *et al.* (1988) and in our figure 9 as $Re_{TW'}$, is that the TW branch ceases to exist by joining another mixed mode state $M'$ which we will discuss in later sections.

### 5.3. *Pure modes*

As stated in § 4, the pure mode branch is created at a circle pitchfork bifurcation to $m = 2$ eigenmodes at $Re_P = 401$. Since the basic branch is unstable to $m = 1$ eigenmodes at this Reynolds number, the pure mode branch is unstable when it first appears. However, as explained in § 3.2.3, this unstable pure mode branch can be followed from its first appearance at $Re_P = 401$ by setting all odd Fourier modes in each velocity component to zero at each time step. The pure mode branch becomes stable at $Re_{M'P} = 452$ via a sequence of bifurcations which we shall discuss below. A stable pure mode state at $Re = 500$ is shown in figure 16($a$). (Pure mode states at lower Reynolds numbers resemble that shown in figure 16.) It is reflection-symmetric,

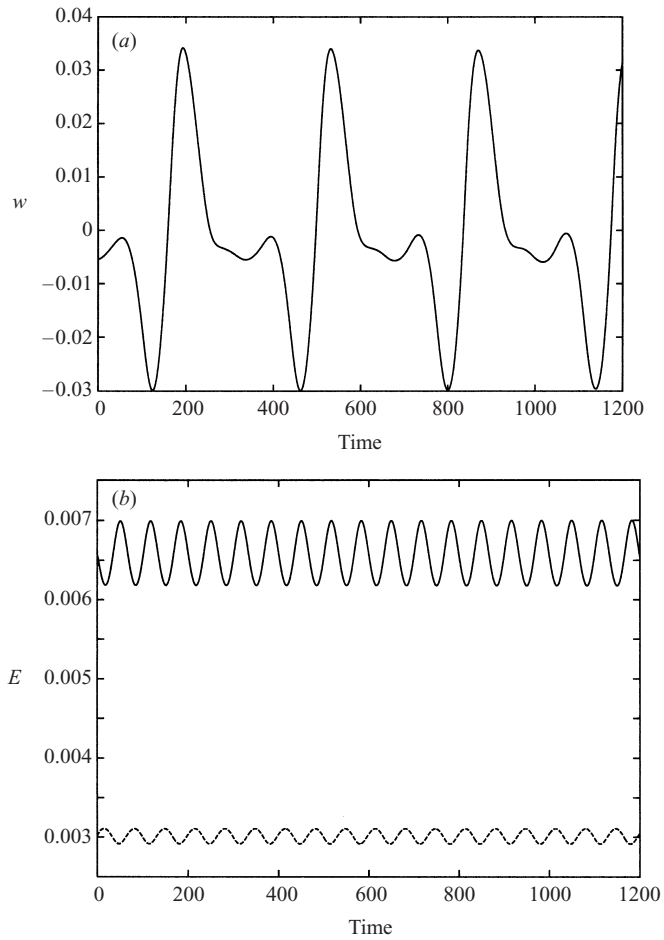


FIGURE 15. Time series corresponding to the modulated waves at $Re = 427.35$. ($a$) Velocity $w(1/2, 0, 0)$. ($b$) Energy components $m = 1$ (solid line) and $m = 2$ (dashed line). The modulation can be seen as the slight variation of the local minima in the velocity signal. The energy components oscillate in phase opposition. The modulation period (seen in the energies) is much smaller than that of the underlying waves (seen in the velocity signal).

i.e. invariant under $R_\pi$, as illustrated in figure 16($a$). The structure consists of the roll-up of the equatorial shear layer in the form of two co-rotating vortices, as shown in figure 16($b$). Therefore, along the equatorial circle, there are two elliptic points around which the flow rotates, separated by two hyperbolic points. These vortices are confined near the sidewall and are manifested in the bulk as a waviness in the shear layer. The inward jet associated with the recirculation zones shown in figure 16($c$) follows the wavy shear layer; i.e. contours of $u$ resemble those of $\omega_r$ in figure 16($d$).

Figure 17 shows the four leading eigenvalues for the basic state for $340 \leqslant Re \leqslant 401$ and for the pure mode states for $Re_P = 401 \leqslant Re \leqslant 452 = Re_{M'P}$. Figure 17 shares many of the features of figure 11. The degeneracy of the eigenvalues $\lambda_1$ and $\lambda_2$ of the basic state is lifted at $Re > Re_P$, where they separate into symmetric and antisymmetric branches. Eigenvalues $2S$ and $2A$ are the bifurcating and neutral modes associated with a circle pitchfork. However, the behaviour in figure 17 is simpler than that of

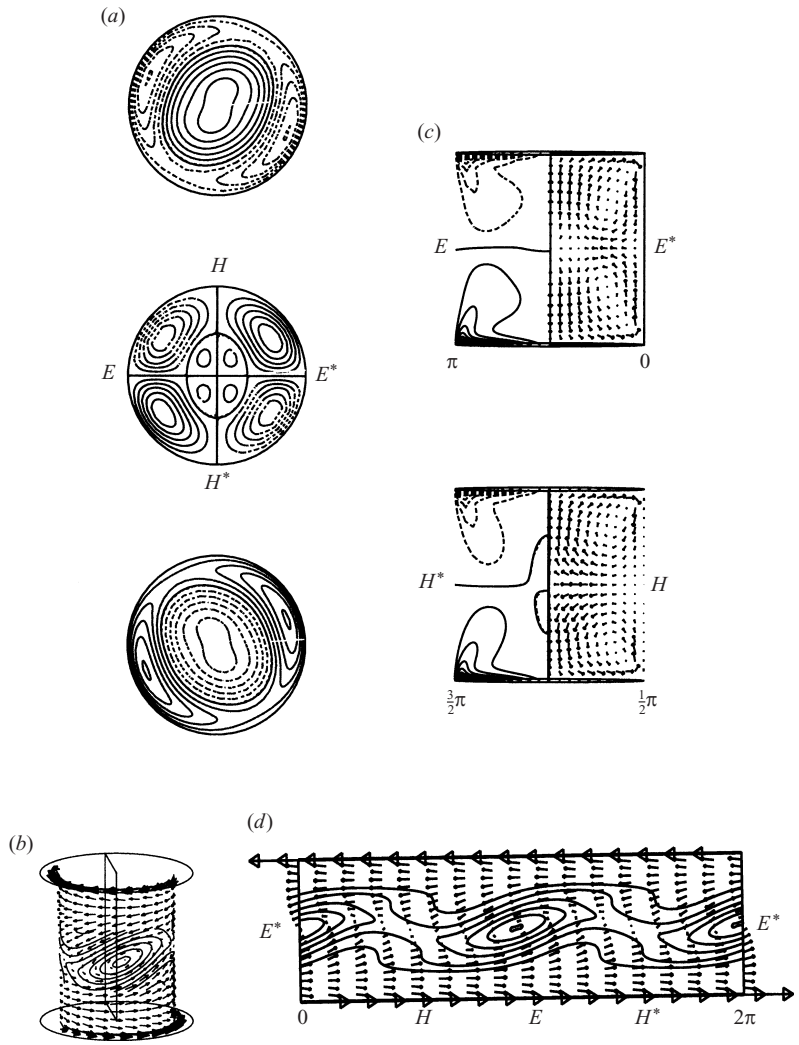


FIGURE 16. The pure mode state at $Re = 500$: ($a$) vertical velocity contours at $z = \Gamma/6$ (top), $z = 0$ (middle), $z = -\Gamma/6$ (bottom). ($b$) Vector field $(v, w)$ and contours of $u$ showing a vortex pair at $r = 0.75$. ($c$) Vector field $(u, w)$ and contours of $v$ at $\theta = 0, \pi$ through the vortices (top) and at $\theta = \pi/2, 3\pi/2$ perpendicularly to the vortices (bottom). ($d$) Unfolded vector field $(v, w)$ and contours of $\omega_r$ at $r = 0.75$. The vortices are centred on elliptic points near $\theta = 0; \pi, z = 0$ and diametrically located from hyperbolic points near $\theta = \pi/2;\ 3\pi/2, z = 0$.

figure 11, due to the constraints imposed by symmetry. The eigenvectors associated with the pure modes (unlike those associated with the mixed modes) remain classifed according to wavenumber: one set contains only odd Fourier modes, the other only even ones. Thus, the eigenvectors have different symmetries. Because of this, they remain decoupled and cannot become complex.

Representative eigenvectors are shown in figure 18. In terms of the normal form (2.5), the pure mode corresponds to $x_2$, with $x_1 = y_1 = y_2 = 0$. Eigenvectors $2S$, $2A$, $1S$ and $1A$ correspond to $x_2$, $y_2$, $x_1$ and $y_1$. (Recall that $x_j$, $y_j$, $z_j$, with subscripts, are used to denote real or complex amplitudes, rather than the spatial coordinate directions.) The pure mode state shown in figure 18 actually possesses two reflection

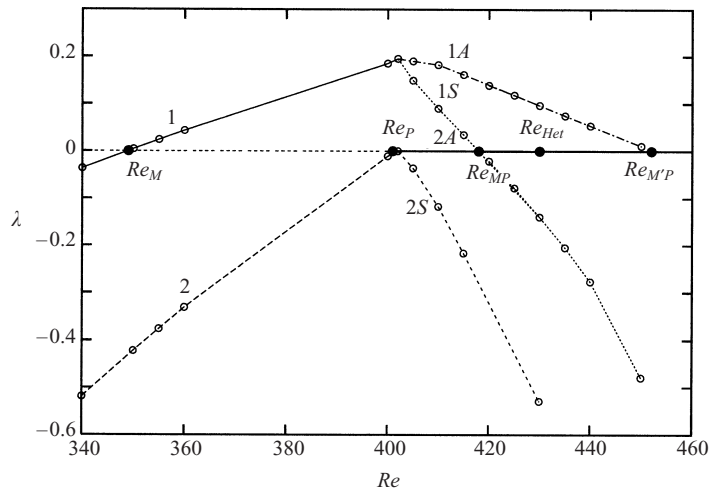


FIGURE 17. The four most dangerous eigenvalues as functions of $Re$ about the basic state for $Re \leqslant Re_P = 401$ and about the pure mode state for $Re_P = 401 \leqslant Re \leqslant Re_{M'P} = 452$. Thresholds are indicated by filled dots: $Re_M = 349$, $Re_P = 401$, $Re_{MP} = 418$, $Re_{Het} = 427.4$, $Re_{M'P} = 452$. For the basic state, the symbols 1 (solid line) and 2 (dashed line) refer to the two-dimensional eigenspaces corresponding to $m = 1$ and $m = 2$, respectively. For the pure mode state, eigenvectors are classified as symmetric ($S$) or antisymmetric ($A$) under $R_\pi$. The $2S$ eigenvalue (short-dashed line) is that which is stabilized by the circle pitchfork and the $2A$ eigenvalue (heavy solid line) is the marginal mode corresponding to rotation. The eigenvalues $1S$ and $1A$, both positive at $Re_P$, become negative at $Re_{MP} = 418$ and $Re_{M'P} = 452$, respectively, above which the pure mode states are stable. At $Re_{Het} = 427.4$, eigenvalues $1S$ and $1A$ are equal and opposite, marking the stabilization of a heteroclinic cycle.

symmetries: combined reflection in $x$ and $z$, i.e. the operator $R_\pi$ defined in (2.3$b$), and also combined reflection in $y$ and $z$. The eigenmodes that we have termed $1S$ and $1A$ in figure 18 are symmetric (antisymmetric) with respect to $R_\pi$.

The eigenvalues $\lambda_{1S}$ and $\lambda_{1A}$ are both positive at $Re_P$. Both must become negative in order for the pure mode branch to be stabilized. Each of these events is associated with a bifurcation. $\lambda_{1S}$ becomes negative at $Re_{MP} = 418$, when the mixed mode branch is destroyed in a pitchfork bifurcation onto the pure mode branch, as mentioned in § 5.1. $\lambda_{1A}$ becomes negative at $Re_{M'P} = 452$, where, according to the analysis of Armbruster *et al.* (1988), another mixed mode $M'$ is created via pitchfork bifurcation from the pure mode branch, finally stabilizing the pure mode branch.

Another bifurcation, labelled $Re_{Het}$ in figure 17, refers to the stabilization of heteroclinic cycles, to which we now turn our attention.

### 5.4. *Heteroclinic cycles*

The most intriguing feature of the 1:2 resonant mode interaction under $O(2)$ symmetry is the existence and stability of heteroclinic cycles over a range of Reynolds number, as described by Armbruster *et al.* (1988) and Proctor & Jones (1988). In their analysis, the branch (torus) of modulated waves arising at $Re_{MWH}$ is destroyed by meeting a heteroclinic cycle at $Re_{Het}$. Indeed, we find that, beyond $Re_{Het} = 427.4$, the solution follows an attracting heteroclinic cycle which links a pure mode $P$ with another dynamically equivalent pure mode $P'$ obtained by rotation of $\pi/2$. Figure 19 shows time series corresponding to the transition from modulated waves to a heteroclinic cycle at $Re = 430$.

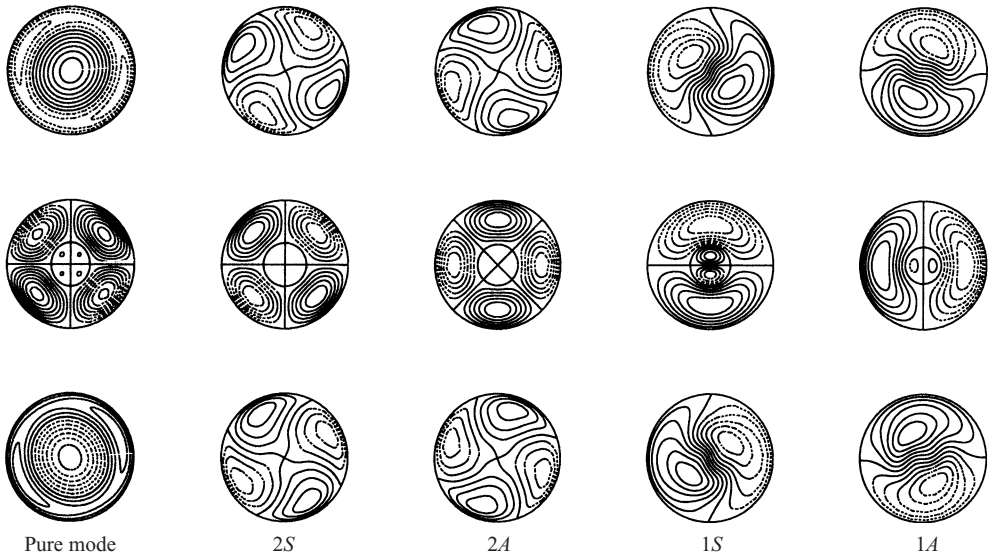


FIGURE 18. Vertical velocity contours at $z = \Gamma/6$ (top), 0 (middle), $-\Gamma/6$ (bottom) for the unstable pure mode at $Re = 410$ and its four most unstable eigenvectors. Positive (negative) contours are indicated by solid (dashed) curves.

The analysis of Armbruster *et al.* (1988) demonstrates that the heteroclinic cycle is controlled by eigenvalues $\lambda_{1S}$ and $\lambda_{1A}$ and corresponding eigenvectors, shown for our flow in figures 17 and 18. The heteroclinic cycle is created at $Re_{MP}$, when $\lambda_{1S}$ becomes negative, but it is unstable. It is stabilized at $Re_{Het}$, when $\lambda_{1S}$ and $\lambda_{1A}$ are equal and opposite and is attracting for $Re_{Het} \leqslant Re < Re_{M'P}$. At $Re_{M'P}$, $\lambda_{1A}$ becomes negative and the pure modes become stable fixed points rather than saddles, thus destroying the heteroclinic cycle.

Figure 20 displays instantaneous flow fields from a heteroclinic cycle connecting pure modes $P$ and $P'$ at $Re = 430$; this heteroclinic cycle is obtained for different initial conditions from that shown in figure 19 (see below). $P$ (figure 20$a, e$) and $P'$ (figure 20$c, g$) each contain two axes of symmetry and oval-like centres. Evolution from $P$ and $P'$ takes place by breaking the symmetry of reflection with respect to the minor axis of the oval. The intermediate phases (figure 20$b, d, f, h$) are characterized by the predominance of $m = 1$ and other odd Fourier components. In each row of figure 20, the flow evolves in the same way, but in a different direction. In the first row, in ($b$i, ii), we see an inner circular $w = 0$ contour moving to the right. In the second row ($d$i, ii) the same circle moves upwards, in the third row ($f$i, ii) it moves leftwards, and in the fourth row ($h$i, ii) it moves downwards.

This heteroclinic cycle is also shown schematically on the left of figure 21, where the labels $a$, $b$, $c$ and $d$ correspond to those used in figure 20. The three normal form amplitudes retained are $(x_1, y_1, x_2)$, corresponding to eigenvenctors $1S$, $1A$, and $2S$. Two pure mode states $P$ and $P'$ are located at diametrically opposite points of the $x_2$-axis ((2.3$a$) and (2.4$a$) show that rotation of the flow field by $\pi/2$ about the vertical axis is represented as multiplication by $-1$ of $z_2$).

The cycle leaves $a$, located in the vicinity of $P$, along its unstable eigenvector $x_1$, which is the stable eigenvector of pure mode $P'$. Rotation of the pure mode state by $\pi/2$ takes place during the rapid phase $b$. The cycle passes through $c$, in the vicinity of the other pure mode state $P'$, then leaves along the unstable eigenvector $y_1$ of $P'$

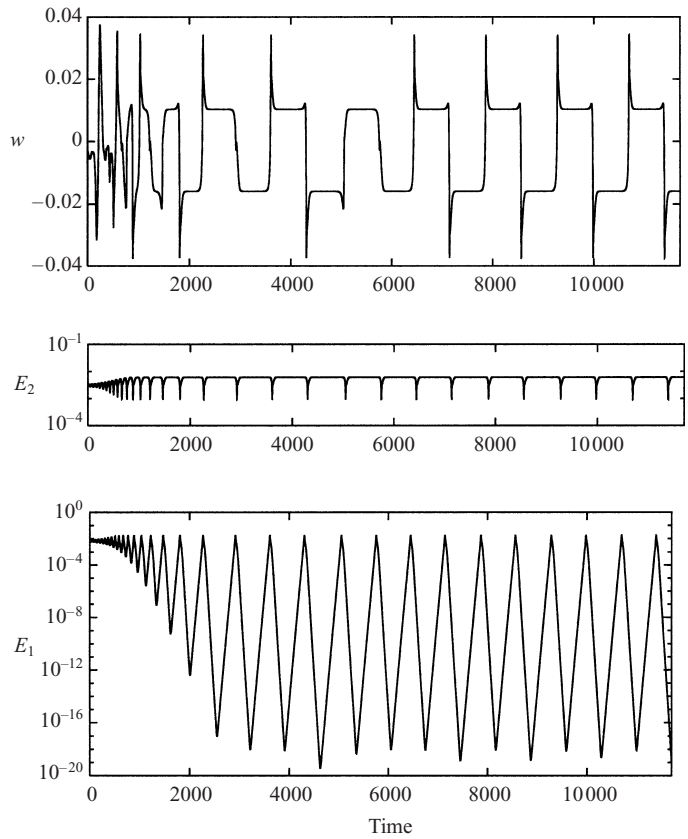


FIGURE 19. Time series corresponding to the approach to a near-heteroclinic cycle at $Re = 430$. Top: Velocity $w(1/2, 0, 0)$. Middle: Energy component $m = 2$ in logscale. Bottom: Energy component $m = 1$ in logscale. The initial sinusoidal modulation of the energy components has a period which is very small compared to that of the underlying rotating wave, as can be seen on the velocity signal. The evolution then becomes highly anharmonic as a near-heteroclinic cycle is approached, and consists of plateaux in $E_2$, separated by phases of alternating exponential growth and decay of $E_1$. Note that the initial conditions for this cycle are different from those of figures 20 and 22.

to undergo a rapid phase $d$. The cycle reapproaches $P$ at a different point, labelled $e$. It then undergoes a rapid phase $f$, approaches $P'$ at point $g$, undergoes another rapid phase $h$, finally returning to $P$ at $a$.

Corresponding time series are shown in figure 22 in linear scale for a vertical velocity signal (top) and in logscale for energy components (middle and bottom). We find that, after transients die out, the oscillation period saturates as is typical of numerical simulations near heteroclinic cycles, due to either noise (Aubry *et al.* 1988) or imperfection (Proctor & Jones 1988). The period is controlled by the time spent in the neighbourhoods of the pure modes $P$ and $P'$, which are saddles, when the energy is dominated by the $m = 2$ component. The time series of $w$ in figure 22 takes the form of four plateaux of equal periods $\tau \simeq 714$, during which the state is very near either $P$ or $P'$, separated by rapid spikes. The period of the near-heteroclinic cycle shown is thus $T \simeq 4\tau = 2856$. The most noticeable feature of the time series of $\log E$ is the alternation between exponential growth and decay of the $m = 1$ component. The positive and negative slopes correspond to eigenvalues $\lambda_{1A} > 0$ and $\lambda_{1S} < 0$,

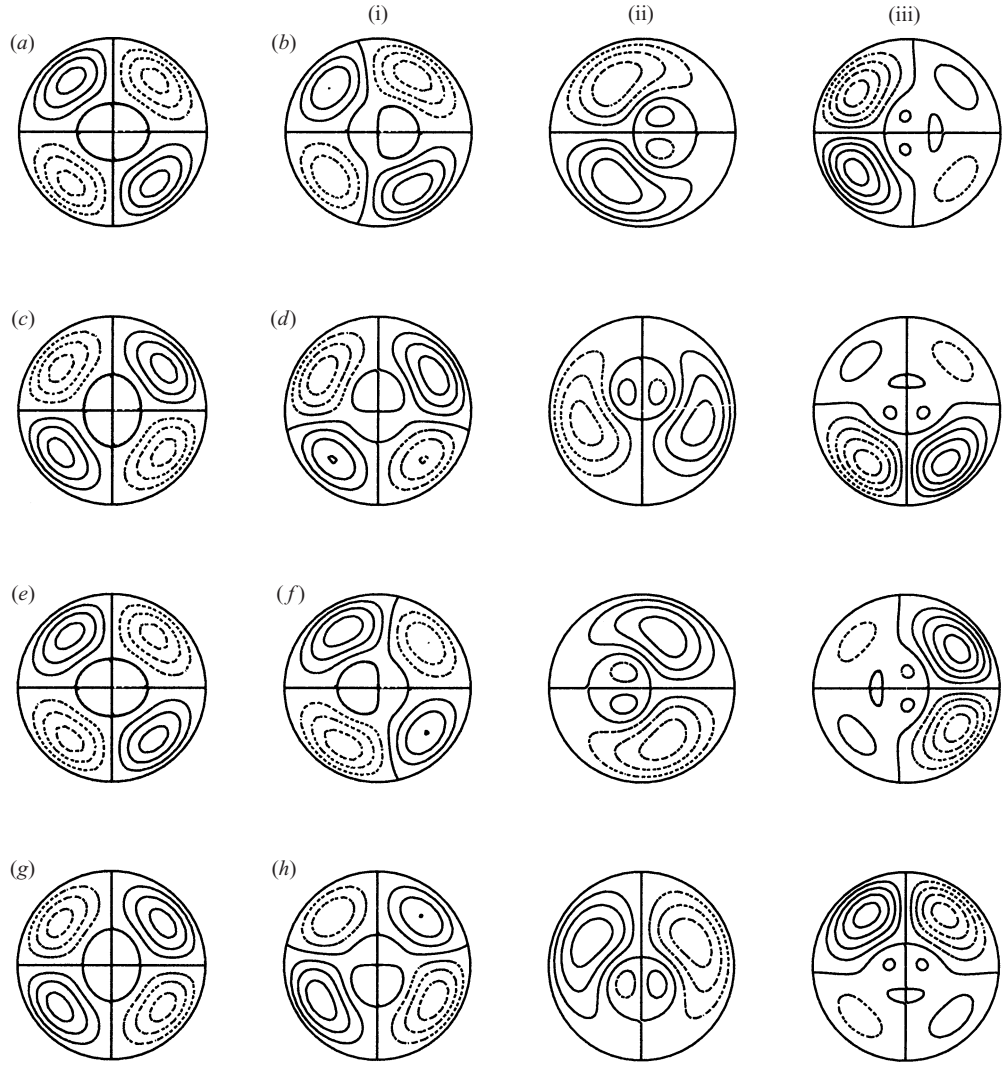


FIGURE 20. Vertical velocity contours at $z = 0$ for a near-heteroclinic cycle at $Re = 430$. The cycle connects the pure mode $P$ in ($a$) with the state $P'$ obtained by rotation of $\pi/2$ in ($c$). Intermediate states, dominated by $m = 1$ and other odd Fourier components, are shown in ($b$), ($d$), ($f$) and ($h$).

respectively. The cycling between the four plateaux is also seen in the slight periodic variation of $m = 1$ energy minima in figure 22.

We have computed another near-heteroclinic cycle at $Re = 435$, visualized in figure 23. This cycle consists of two plateaux rather than four. Figure 24 displays the temporal evolution of a typical velocity and of the energy in the $m = 1$ and $m = 2$ components. Two plateaux per cycle can be seen, each of length $\tau \simeq 900$ and the total period is $T \simeq 2\tau = 1800$. The two plateaux again appear as two minima of slightly different magnitudes in the $m = 1$ energy component of figure 24. Thus, the approach to $P'$ is closer than that to $P$ in this 'shadowing' of the heteroclinic cycle. (In contrast, in the case of four plateaux, the near-heteroclinic cycle passes closer to $P$ and to $P'$, and then farther from each.) This cycle is depicted schematically as the right-hand

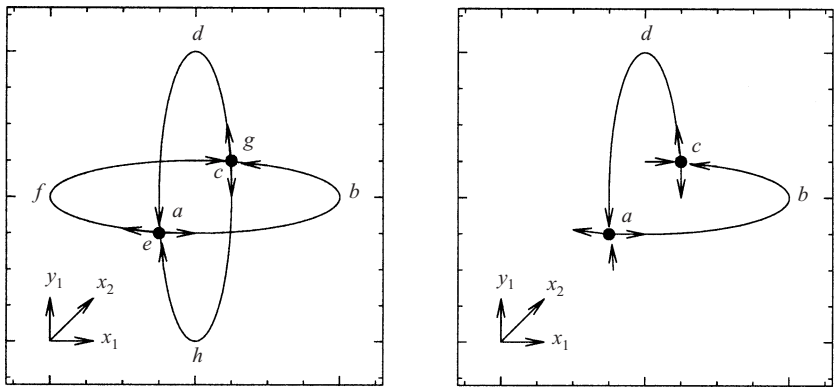


FIGURE 21. Schematic phase portraits of heteroclinic cycles. The three dimensions retained are $(x_1, y_1, x_2)$ of the normal form (2.5). Left: A four-plateau cycle; right: a two-plateau cycle. The two pure mode states, $P$ and $P'$, labeled as $a$ and $c$ and related by rotation by $\pi/2$, are located at diametrically opposite points of the $x_2$-axis. $b$ and $d$ label portions of the cycle during which the flow undergoes rapid rotation by $\pi/2$. The unstable eigenvector of $a$ is in the $x_1$-direction, that of $c$ along the $y_1$ direction. In the four-plateau diagram on the left, the cycle traverses $a$, $b$, $c$, $d$, $e$, $f$, $g$, $h$. In the two-plateau diagram on the right, it traverses $a$, $b$, $c$, $d$. Labels correspond to those in figures 20, 22, 23 and 24.

half of figure 21. After passing through $a$, $b$, $c$ and $d$, the cycle reapproaches $P$ at $a$ and the cycle then repeats.

The difference between the two types of heteroclinic cycles would seem to be determined by a combination of Reynolds number and the choice of the initial conditions. Table 1 summarizes the types of heteroclinic cycles we have obtained. The initial conditions are of two types. One type, which we term straight alignment, is a pure mode state whose symmetry axes are oriented along $\theta = 0, \pi/2, \pi, 3\pi/2$ as in figure 20. Noise of amplitude $5 \times 10^{-9}$ is added to the $m = 1$ Fourier component of the azimuthal velocity of the initial condition at each spatial point. (The maximum value of the azimuthal velocity is one, by virtue of our non-dimensionalization.) The other type of initial condition, which we term arbitrary alignment, is a travelling wave computed at a smaller Reynolds number as in figure 23.

At $Re = 428$, we have obtained only heteroclinic cycles with four plateaux. At $Re = 430$, we have obtained cycles with either four plateaux, or with two plateaux. The initial condition for the cycle with four plateaux, shown in figures 20 and 22 is a pure mode with straight alignment. When instead an initial condition of arbitrary alignment is used at $Re = 430$, the cycle eventually contains two plateaux rather than four, as shown in figure 19. At $Re = 435$, we obtain heteroclinic cycles containing two plateaux, such as that shown in figures 23 and 24, for initial conditions of either alignment.

The symmetry axes are theoretically of no importance, but the numerical spatial discretization could be responsible for enforcing an invariant subspace associated with symmetry axes $\theta = 0$, $\pi/2$, $\pi$, $3\pi/2$ for the $m = 2$ Fourier component which is not maintained for arbitrary off-centred symmetry axes.

Table 1 also demonstrates other quantitative properties of these numerical approximations to heteroclinic cycles. The duration $\tau$ of each plateau increases with $Re$, while the minimum of $E_1$ decreases as $Re$ is increased. There are also slight differences in $\tau$ and $E_1$ between cycles of straight and arbitrary alignment. For a genuine heteroclinic cycle, $\tau$ would increase and $E_1$ would decrease without bound for each simulation, approaching infinity and zero, respectively, rather than saturating at the finite values

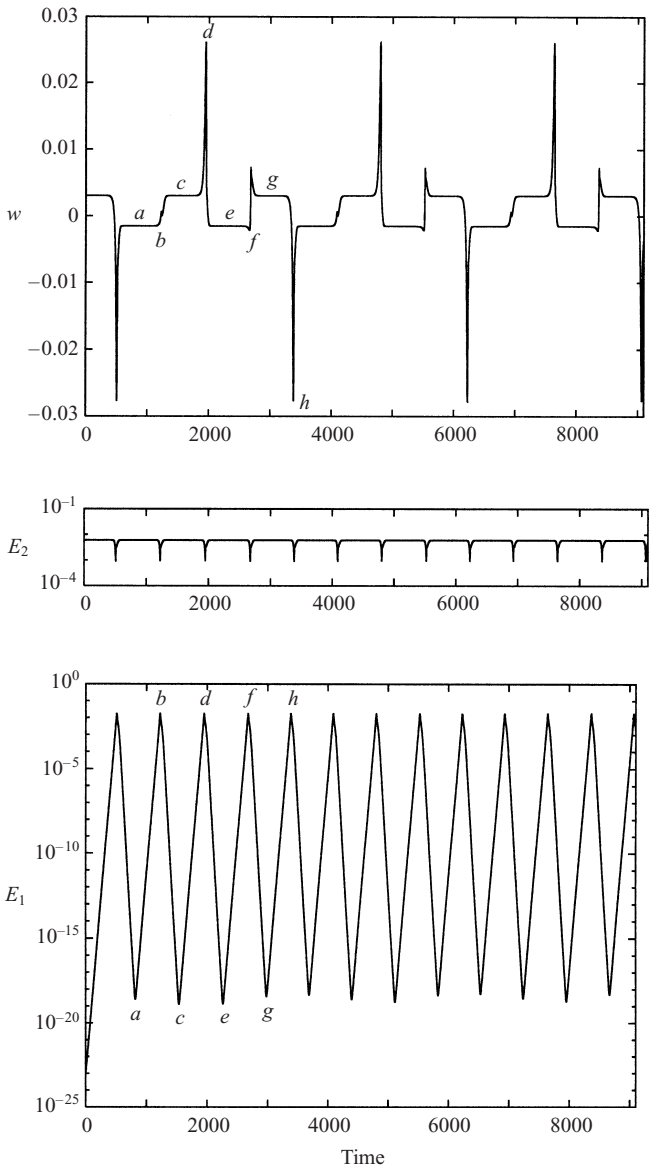


FIGURE 22. Time series corresponding to a near-heteroclinic cycle at $Re = 430$. Top: Velocity $w(1/2, 0, 0)$. Middle: Energy component $m = 2$ in logscale. Bottom: Energy component $m = 1$ in logscale. The near-heteroclinic cycle consists of four plateaus separated by rapid spikes and has period $T \simeq 2856$. Note that the initial conditions for this cycle are different from those of figure 19. The exponential growth and decay of the $m = 1$ energy component correspond to $\lambda_{1A}$ and $\lambda_{1S}$, respectively, which are the unstable and the weakest stable eigenvalues of the pure mode branch.

shown. For the run at $Re = 435$ described in the last line of table 1, we have carried out a simulation with a smaller timestep $\Delta t = 0.5 \times 10^{-2}$. This run yielded periods $\tau$ which differed by less than 0.33% from those obtained with $\Delta t = 10^{-2}$.

### 5.5. *Final comments on bifurcation sequence*

We recapitulate our results by showing a quantitative bifurcation diagram corresponding to the schematic diagram shown as figure 9. Figure 25 shows the square root of the

| $Re$ | Alignment | Plateaux | Duration $\tau$ | min $E_1$ | Figures |
|---|---|---|---|---|---|
| 428 | Straight | 4 | 550 | $10^{-14}$ | Not shown |
| 428 | Arbitrary | 4 | 550 | $10^{-14}$ | Not shown |
| 430 | Straight | 4 | 714 | $10^{-19}$ | 20, 22 |
| 430 | Arbitrary | $4 \rightarrow 2$ | 710 | $10^{-19}$–$10^{-18}$ | 19 |
| 435 | Straight | 2 | 930 | $10^{-24}$–$10^{-23}$ | Not shown |
| 435 | Arbitrary | 2 | 900 | $10^{-23}$–$10^{-22}$ | 23, 24 |

TABLE 1. Heteroclinic cycles. Depending on the Reynolds number ($Re$) and the alignment (straight or arbitrary) of the initial pure mode, the cycle may have four or two plateaux. As $Re$ is increased, the duration $\tau$ of each plateau increases and minimum value of $E_1$ decreases.

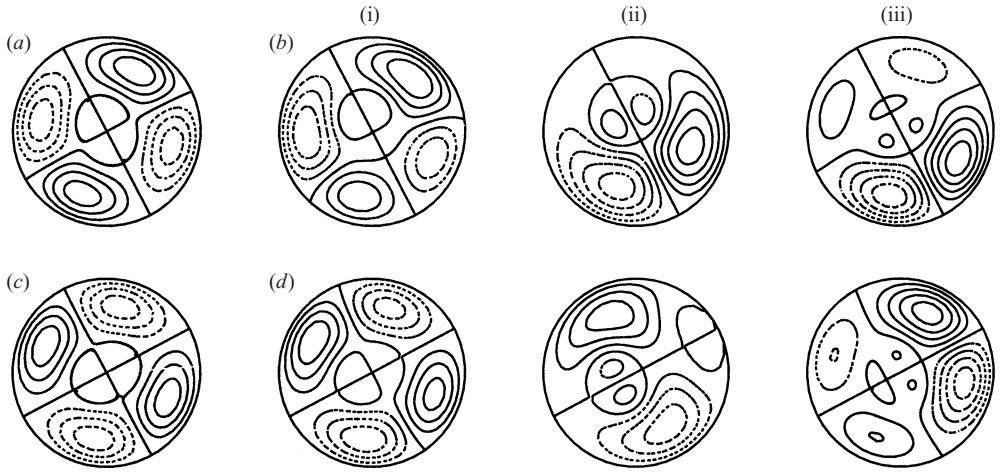


FIGURE 23. Vertical velocity contours at $z = 0$ for a near-heteroclinic cycle at $Re = 435$. The cycle connects pure modes $P$ ($a$) and $P'$ ($c$), related by rotation of $\pi/2$. Intermediate states, dominated by $m = 1$ and other odd Fourier components, are shown in ($b$) and ($d$).

total energy for all the states which we have computed. It shows the pure mode branch starting at $Re = 401$ and meeting the mixed mode branch at $Re_{MP} = 418$. The energy of the travelling wave states which are stable for $412 = Re_{TW} \leqslant Re \leqslant Re_{MWH} = 427.3$ is constant and lies above the mixed and pure mode branches. The energy of the periodic near-heteroclinic cycles which are stable for $Re_{Het} = 427.4 \leqslant Re \leqslant Re_{M'P} = 452$ is time-dependent, but is equal during almost the entire period to that of the unstable pure mode branch.

Despite using only time-integration of the nonlinear and of the linearized Navier–Stokes equations, we have been able to calculate almost all of the dynamical states and eigenvectors of interest by imposing symmetries indicated by the simulations and the normal form. There are two exceptions, which can be seen as the dot-dashed curves in the schematic bifurcation diagram of figure 9 which are absent from the quantitative bifurcation diagram of figure 25. The first exception is the mixed mode branch $M'$ which is necessarily created at $Re_{M'P} = 452$ when the eigenvalue $\lambda_{1A}$ crosses zero, stabilizing the pure mode branch. Even without computing the $M'$ branch, we have been able to draw sufficient conclusions to justify drawing the branch as we have done in figure 9. First, $M'$ necessarily branches to the right from $Re_{M'P}$, since otherwise it would be stable and observed in our simulations. Secondly, branch $M'$ does not

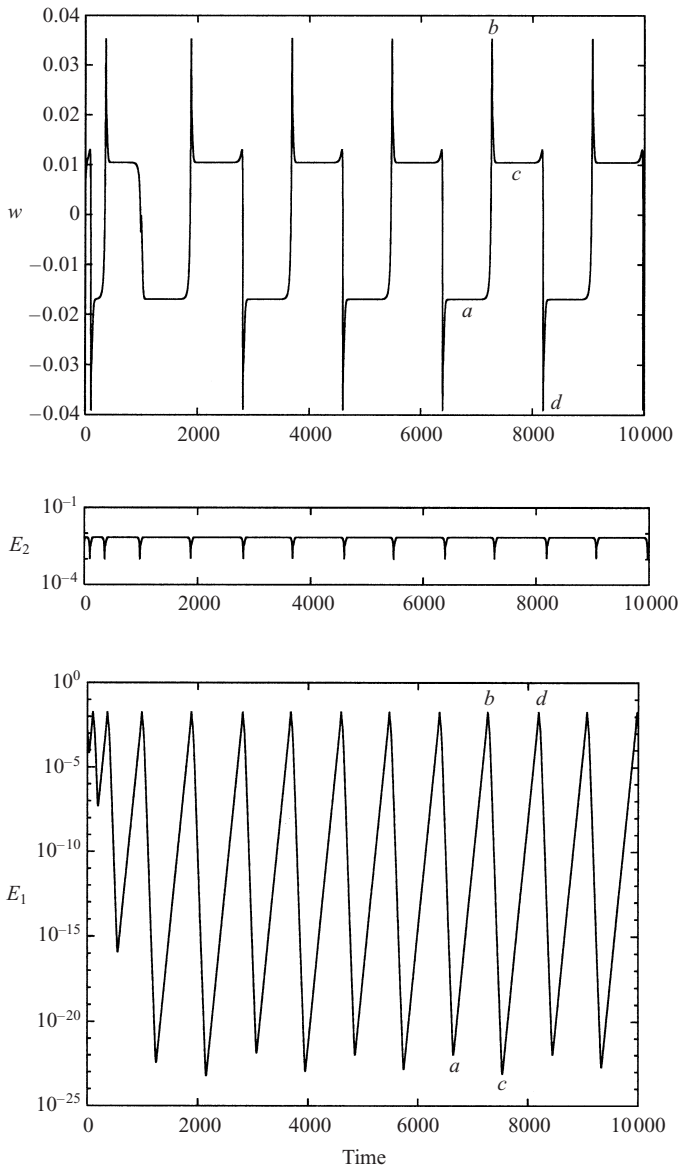


FIGURE 24. Time series corresponding to a near-heteroclinic cycle at $Re = 435$. Top: Velocity $w(1/2, 0, 0)$. Middle: Energy component $m = 2$ in logscale. Bottom: Energy component $m = 1$ in logscale. The near-heteroclinic cycle consists of two plateaux separated by rapid spikes and has period $T \simeq 1800$. The exponential growth and decay of the $m = 1$ energy component correspond to $\lambda_{1A}$ and $\lambda_{1S}$, respectively, which are the unstable and the weakest stable eigenvalues of the pure mode branch.

intersect the basic state in a pitchfork bifurcation analogous to $Re_M$, although this occurs in the full $(\mu_1, \mu_2)$ unfolding of the 1:2 resonance. We know that our path through the $(\mu_1, \mu_2)$ parameter space does not take us through this bifurcation, since the linear stability analysis displayed in figure 8, together with a calculation via the Arnoldi method of the next leading $m = 1$ eigenpair, shows no evidence of a second bifurcation of $m = 1$ modes for $Re \leqslant 1000$. The second branch we have been

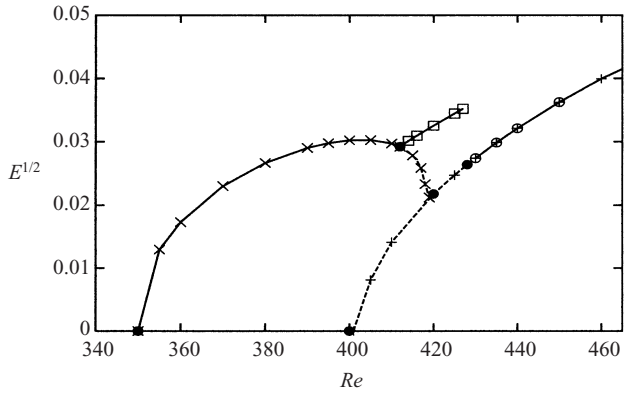


FIGURE 25. Square root of total energy as a function of *Re*. Stable solutions are indicated by solid curves and unstable ones by dashed curves. ×, $M$ modes; □, $TW$; +, $P$ modes; ○, near-heteroclinic cycles. Thresholds are indicated by dots.

unable to compute is the travelling-wave branch above $Re_{MWH} = 427.3$, where it loses stability via a Hopf bifurcation. The travelling waves are neither axisymmetric nor reflection-symmetric, and so the Hopf bifurcation cannot be suppressed by imposing any spatial symmetry.

The $M'$ mixed mode branch could in principle be calculated via standard continuation techniques using a matrix-free Newton's method, as was done for the axisymmetric steady states; see § 3.2.1. The unstable travelling-wave branch could also be calculated in this way by solving simultaneously for the rotating frame in which it appears as a steady solution. However, the inexact imposition of incompressibility via pressure projection in the non-axisymmetric time integration code (see § 3.1.3) renders problematic its adaptation to carry out Newton's method.

In figure 26, we present a schematic phase diagram like that in Armbruster *et al.* (1988) of the unfolding of the codimension-two point $\mu_1 = \mu_2 = 0$. Figure 26 includes the (schematic) path in the $(\mu_1, \mu_2)$-plane which is followed by our von Kármán flow as the Reynolds number is increased. We have used the expressions in Armbruster *et al.* (1988) for the bifurcation sets:

$$M : \mu_1 = 0,\ \mu_2 < 0, \tag{5.2a}$$

$$P : \mu_2 = 0, \tag{5.2b}$$

$$TW : \mu_2 = \frac{d}{c}\mu_1 + \frac{-e}{2c^2}\left(1 - \sqrt{1 - 4c\mu_1}\right), \tag{5.2c}$$

$$MP : \mu_1 = \frac{\mu_2}{b} + \sqrt{\frac{\mu_2}{-e_{22}}}, \tag{5.2d}$$

$$MWH : \mu_2 = a\mu_1, \tag{5.2e}$$

$$Het : \mu_2 = b\mu_1, \tag{5.2f}$$

$$M'P : \mu_1 = \frac{\mu_2}{b} - \sqrt{\frac{\mu_2}{-e_{22}}}, \tag{5.2g}$$

$$TW' : \mu_2 = \frac{d}{c}\mu_1 + \frac{-e}{2c^2}\left(1 + \sqrt{1 - 4c\mu_1}\right), \tag{5.2h}$$

$$M' : \mu_1 = 0,\ \mu_2 > 0, \tag{5.2i}$$

$$SW : \mu_2 \approx -3e_{22}\mu_1^2, \tag{5.2j}$$

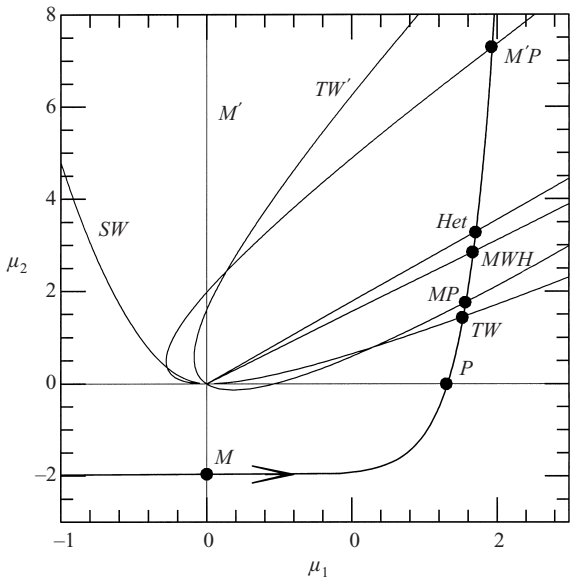


FIGURE 26. Phase diagram. Curves in the $(\mu_1, \mu_2)$-plane show bifurcation loci for the normal form. The heavy curve shows schematically a path corresponding to increasing $Re$ in our fluid-dynamical simulations of the von Kármán flow. The bifurcations we observe correspond to intersections of the path with the bifurcation loci and are indicated by dots. Bifurcations from basic state to mixed modes $M$ and pure modes $P$, from mixed modes to travelling waves $TW$, joining mixed and pure modes $MP$, from travelling waves to modulated travelling waves $MWH$, from modulated travelling waves to heteroclinic orbits Het, and joining mixed and pure modes $M'P$, and terminating the travelling waves $TW'$ are encountered sequentially. Bifurcation loci in the normal form which appear on the diagram but either are not traversed by our path or are not directly observed are from the basic state to mixed mode $M'$, terminating the travelling waves $TW'$, and from mixed modes to standing waves $SW$.

where the coefficients $a$, $b$, $c$, $d$ and $e$ are derived from the normal form quantities $e_{11}$, $e_{12}$, $e_{21}$, $e_{22}$ of (2.5) via

$$b = \frac{e_{22}}{e_{12}}, \quad c = 2e_{11}+e_{12}, \quad d = 2e_{21}+e_{22}, \quad e = 2c+d, \quad a = 1+\frac{9(e_{22}-e_{12})}{e-3(e_{22}-e_{12})}. \tag{5.3}$$

We have set

$$e_{11} = -1, \quad e_{12} = -0.9, \quad e_{21} = -3, \quad e_{22} = -1.6, \tag{5.4}$$

since we have found that these values reproduce the sequence of bifurcations computed numerically and shown in bifurcation diagrams 9 and 25.

Our computations coincide very closely with the analysis of the normal form by Armbruster *et al.* (1988) and Proctor & Jones (1988). The very large number of degrees of freedom in the hydrodynamic system or its numerical discretization could thus be interpreted as damped modes which are 'slaved' to the four components of the normal form (2.5). We mention here the few curious features that may merit further investigation.

It is intriguing that five eigenvalues are necessary to account for all three bifurcations undergone by the mixed mode at $Re_M$, $Re_{TW}$, and $Re_{MP}$, as described in § 5.1. This feature moderates the interpretation of our von Kármán flow as a faithful realization of the four-dimensional normal form (2.5). Although the behaviour at each of $Re_M$, $Re_{TW}$, and $Re_{MP}$ is as predicted from the normal form, it is not possible to pass

continuously through all three bifurcations while retaining only a four-dimensional system. Other eigenvalues of the hydrodynamic system are sufficiently close to the four critical eigenvalues to become entangled with them, possibly because of the distance of our system from the codimension-two point.

In the analysis of Armbruster *et al.* (1988), modulated waves exist between the Hopf bifurcation at $Re_{MWH}$ and the global bifurcation at $Re_{Het}$ and are stable if $Re_{MWH} < Re_{Het}$. In our case $Re_{MWH} = 427.3$, as determined by measuring the growth and decay rates of sinusoidal modulations, and $Re_{Het} = 427.4$, as determined by the criterion that the leading non-zero eigenvalues be equal and opposite. It is clear, however, that our case is very close to a codimension-two point at which $Re_{MWH}$ and $Re_{Het}$ coincide.

In the normal form analysis, the heteroclinic cycles may be destroyed by colliding with standing waves which are themselves generated at a Hopf bifurcation from a mixed mode branch. This is not a necessary part of the scenario; its presence will depend on the path taken through the $(\mu_1, \mu_2)$-plane. We see no evidence of standing waves in our simulations.

The main question is that of different types of near-heteroclinic cycles. We obtain timeseries consisting of four or two plateaux, depending on the Reynolds number and the axis of symmetry of the initial conditions. Mercader *et al.* (2001) have conducted simulations of weakly non-Boussinesq Rayleigh–Bénard convection in two spatial dimensions. (The Boussinesq approximation leads to an additional $Z_2$ symmetry, for which the 1:2 codimension-two normal form excludes the quadratic terms in (2.5) which produce the interesting dynamics, cf. Armbruster (1987) and Cox (1996).) The near-heteroclinic cycles produced by these simulations depend on the Rayleigh number just as ours do on the Reynolds number: at parameter values near the transition from modulated waves to heteroclinic cycles, cycles with four plateaux are produced, while further from the transition, the cycles have two plateaux. These authors describe four-plateau and two-plateau cycles as possessing rotating phase and trapped phase, respectively.

Mercader *et al.* (2001) also discovered near-heteroclinic cycles in which the phase of the $m = 1$ component alternates chaotically rather than regularly. In contrast, we have not observed chaotic behaviour in any of our near-heteroclinic cycles. These authors raise a number of basic questions about the near-heteroclinic cycles, concerning the presence and causes of chaos, the saturation of the period in numerical simulations, and the role of the phase or alignment in the initial conditions. They even conjecture that the heteroclinic cycles, whose existence has been proved only for the normal form, may actually not exist for higher-dimensional realizations of the 1:2 resonance, although 'ghosts' of them would remain present. The stability of the cycles, if they exist, has, in contrast, been proven for higher-dimensional systems (Krupa & Melbourne 1995).

Although further investigation of the heteroclinic cycles in our system would be desirable, these simulations are extremely time-consuming. The heteroclinic cycles discussed in § 5.4 each required between 40 and 110 CPU hours on a NEC-SX5 supercomputer with a speed of 5 Gflops, making systematic investigation unfeasible.

## 6. Physical mechanisms

In this section, we discuss the basic axisymmetric flow in the context of the early theoretical analysis of flow above a single rotating disk or between two disks of infinite radius. We will then propose a physical mechanism for the instability to non-axisymmetric flows that we have observed in our numerical simulations.

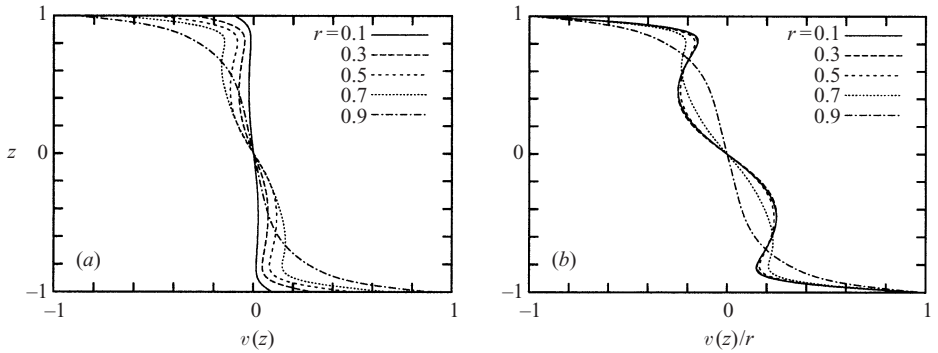


FIGURE 27. Typical azimuthal profiles of the axisymmetric basic state at $Re = 355$: (*a*) $v(r,z)$ at different radii as indicated; (*b*) $v(r,z)/r$ at different radii as indicated. The similarity zone, defined as the region in which the profiles $v(r,z)/r$ depend only slightly on $r$, extends from $r = 0$ to $r = 0.5$.

Historically (von Kármán 1921; Batchelor 1951), the axisymmetric flow between differentially rotating disks of infinite radial extent ($\Gamma = 0$) was shown to be described by a similary solution in which the fluid 'disk' at each height $z$ rotates with an angular velocity which is a function of $z$. That is, each fluid disk carries out solid-body rotation. When $\Gamma$ is greater than zero, this remains approximately true over a radial range sufficiently far from the bounding cylinder (Cousin-Rittemard *et al.* 1998). In figure 27, we show the azimuthal velocity $v(r,z)$ and angular velocity $v(r,z)/r$ profiles for the basic flow at $Re = 355$ as a function of $z$ for radii ranging from 0.1 to 0.9. Figure 27(*b*) shows that for $Re = 355$, a similarity zone exists over $0 \leqslant r \leqslant 0.5$, in which $v(r,z)/r$ depends only weakly on $r$. The same is true for the azimuthal velocity profiles at $Re = 410$, which greatly resemble those at $Re = 355$. For both $Re = 355$ and $Re = 410$, the maximum azimuthal velocity is 7–8 times greater than the maximum radial or axial velocities, providing a quantitative justification for a qualitative description of the flow as consisting of a dominant azimuthal shear layer and second-order recirculation zones. Indeed, Lopez *et al.* (2002) established that the dynamics of this system are dominated by the free shear layer lying between two regions of opposite azimuthal velocity, confirming the hypothesis previously proposed by Lopez (1998).

We now put forth an interpretation of the mechanism of the instability of the basic flow. Figure 28 shows the spatial distribution of the energy of the eigenvectors responsible for the $m = 1$ and $m = 2$ bifurcations. The localization of this energy around the $z = 0$ mid-plane suggests that the cause of the instability is to be found in the nature of the basic flow in this region. The vortical structures seen near the mid-plane in the mixed and pure modes shown in figures 10 and 16 bear a resemblance to the chain of co-rotating vortices, sometimes called cat's eyes, seen in the Kelvin–Helmholtz instability. The Kelvin–Helmholtz instability is a two-dimensional instability of a one-dimensional velocity profile $u(y)\boldsymbol{e}_x$ to eigenmodes of the form $(u'(y)\boldsymbol{e}_x + v'(y)\boldsymbol{e}_y)\,\mathrm{e}^{\mathrm{i}\alpha x}$. Betchov & Szewczyk (1963) studied the instability of the classic shear layer profile

$$u(y) = U\tanh(y/\delta), \tag{6.1}$$

which serves as the paradigm for the Kelvin–Helmholtz instability. Betchov & Szewczyk (1963) plot the marginal stability curve in the $(Re_{KH}, \alpha)$-plane, where $Re_{KH} = U\delta/\nu$ and $\alpha$ is given in units of $\delta^{-1}$.

We seek to adapt this analysis in our case to describe the instability of a velocity

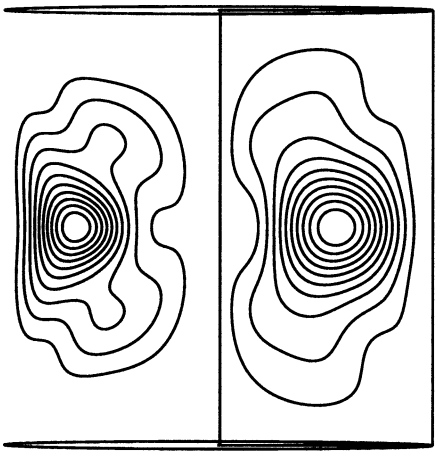

FIGURE 28. Energy contours for the $m = 2$ at eigenvector at $Re = 410$ (left-hand side) and the $m = 1$ eigenvector at $Re = 355$ (right-hand side).

profile $v(z)\boldsymbol{e}_\theta$ to eigenmodes of the form $(v'(z)\boldsymbol{e}_\theta + w'(z)\boldsymbol{e}_z)\,\mathrm{e}^{\mathrm{i}m\theta}$, treating the weaker radial dependence as parametric. For $r \lesssim 0.75$, i.e. except near the outer cylinder, the profiles in figure 27 present vertical tangents in the $v/r$ profiles at $z \approx \pm 0.4$. The central range $-0.4 \leqslant z \leqslant 0.4$ of the profiles can be fitted to the central portion of a hyperbolic tangent function:

$$v(r, z)/r = \omega(r)\ \tanh(z/\delta(r)). \tag{6.2}$$

In our analysis, $Re_{KH}$ and $\alpha$ depend on $r$, and the wavelength is quantized by the finite circumference of the cylinder. In our units and geometry,

$$Re_{KH}(r) = r\omega(r)\delta(r)Re, \tag{6.3a}$$

since $\nu = 1/Re$, with $Re$ defined by (2.1*b*), and

$$\alpha(r) = \delta(r)m/r, \tag{6.3b}$$

since the circumference corresponding to an azimuthal wavenumber $m$ at a radius $r$ is $2\pi r/m$. The values of $\delta(r)$ and $\omega(r)$ obtained in this way are both about 0.3. ($\delta$ decreases from 0.29 for $Re = 350$ to 0.24 for $Re = 500$, while $\omega$ increases from 0.27 for $Re = 350$ to 0.35 for $Re = 500$.)

We calculate $\omega(r)$ and $\delta(r)$ for the basic axisymmetric velocity fields at $Re = 300$, $Re = 350$, and $Re = 400$, which are below, near, and above the $m = 1$ instability threshold. We then calculate $\alpha(r)$ and $Re_{KH}(r)$ via (6.3*a*)–(6.3*b*). In figure 29(*a*), we plot these points. We also plot the marginal stability curve of Betchov & Szewczyk (1963); the Kelvin–Helmholtz unstable region is below the curve.

It can be seen that, for $Re = 300$, the curve $(Re_{KH}(r), \alpha(r))$ is almost tangent to the Kelvin–Helmholtz marginal stability curve at $r = 0.6$, but lies primarily in the stable region. For $Re = 350$, the curve $(Re_{KH}(r), \alpha(r))$ lies in the Kelvin–Helmholtz unstable region for $r > 0.45$. For $Re = 400$, the range $r > 0.4$ of the curve $(Re_{KH}(r), \alpha(r))$ lies deeper within the unstable region.

Many factors complicate this application of the Kelvin–Helmholtz instability. One factor is the finite width in $r$ occupied by the instability. The usual analysis of the Kelvin–Helmholtz instability assumes an infinite extent in the spanwise direction $z$, which is analogous to $r$ in our analysis. The Kelvin–Helmholtz instability cannot thrive

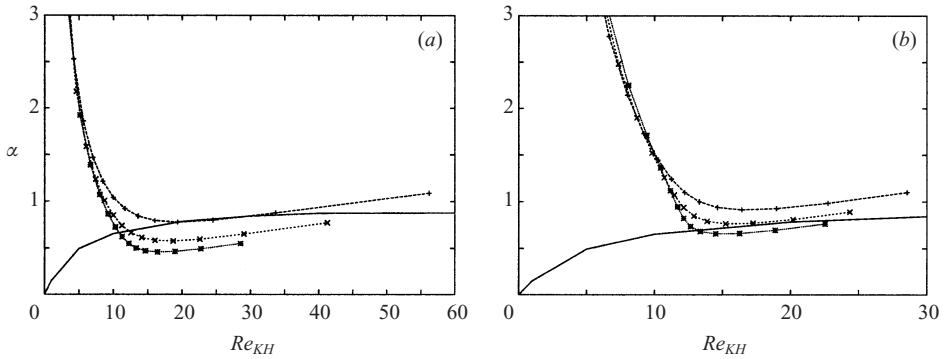


FIGURE 29. Wavenumber $\alpha$ (in units of the inverse shear layer thickness) as a function of $Re_{KH}$ computed for (*a*) $m = 1$ and (*b*) $m = 2$ together with the marginal stability curve of Betchov & Szewczyk (1963) (shown as a continuous line). In (*a*), from top to bottom, $Re = 300$, 350, 400 and in (*b*), $Re = 400$, 450, 500. Points correspond to $r$ values of 0.75, 0.7, ... 0.1.

in an infinitesimal spanwise (or radial) slice, because of damping due to spanwise (radial) gradients. This damping would justify the fact that the instability threshold we observe occurs at $Re = 349$, where much of the curve $(Re_{KH}(r), \alpha(r))$ lies in the unstable region, rather than at $Re = 300$, where the curve barely penetrates it. We may introduce the heuristic criterion that instability occurs when the unstable radial range occupies a width $2\delta(r)$. Other factors neglected by this analysis, which are more difficult to take into account heuristically, are the radial and axial components of the basic flow. The axial component $w$ of the basic flow is zero at the mid-plane, as required by symmetry and shown in figure 2, and hence small in the equatorial region. The radially inward jet at the equator, also shown in figure 2 is, however, not small, with $u \approx -0.06$ to be compared with the azimuthal component of order $v \approx 0.15$ in the shear layer. We have also neglected curvature. Finally, it should be recalled that the analysis of Betchov & Szewczyk (1963) is itself approximate. Since (6.1) is not an exact solution to the Navier–Stokes equations, their analysis can be interpreted as describing a system in which an external force is added which maintains the shape and intensity of the profile (6.1).

The same analysis can be carried out for the $m = 2$ instability. Figure 29(*b*) shows $(Re_{KH}(r), \alpha(r))$ for the basic axisymmetric velocity fields at $Re = 400$, $Re = 450$, and $Re = 500$, with $\alpha(r)$ calculated via (6.3*b*), this time using $m = 2$. The curve $(Re_{KH}(r), \alpha(r))$ for $Re = 400$ lies above the Kelvin–Helmholtz instability boundary, that for $Re = 450$ almost tangent to the instability boundary, and that for $Re = 500$ inside the instability boundary for $r > 0.5$. Our analysis is less successful in this case, since the $m = 2$ instability we observe occurs at $Re = 401$, a value for which the curve $(Re_{KH}(r), \alpha(r))$ is everywhere outside the Kelvin–Helmholtz instability boundary.

It is possible that the study closest to our parameter values, that of Lopez *et al.* (2002) for $\Gamma = 0.5$ and $s = -0.8$ (and $\boldsymbol{v} = 1$ at $r = 1$ instead of $\boldsymbol{v} = 0$) may also be amenable to this analysis. If the height $\delta(r)$ of the shear layer occupied a constant proportion of the cylinder height, then the values of $\delta(r)$ for $\Gamma = 0.5$ would be a quarter of our value for $\Gamma = 2$. In order to achieve the same values of $Re_{KH}$ and $\alpha$ in (6.3*a*)–(6.3*b*) that we have observed, each of $Re$ and $m$ would need to be multiplied by 4. Indeed, Lopez *et al.* (2002) observe competition between $m = 4$ and $m = 5$ patterns. The critical Reynolds number, however, is smaller than $4 \times 350 = 1400$, since their patterns were observed at $Re = 1000$. (They did not determine a Reynolds number threshold for fixed $s$, but instead fixed $Re = 1000$ and

varied $s$.) The scaling $m \sim 2/\Gamma$ of the first instability for the strongly counter-rotating case does not require the detailed Kelvin–Helmholtz mechanism that we have postulated but the much weaker hypothesis that the instability is localized in a shear layer occupying a constant proportion of the height, leading to an azimuthal wavelength which is half of the height.

Although our analysis is quite crude, the critical Reynolds number it predicts is fairly accurate for the $m = 1$ instability although it overestimates the $m = 2$ instability threshold by 20–40%. It is clear that the instability we observe is centred in the equatorial region; our Kelvin–Helmholtz analysis provides a mechanism for setting the axial and the azimuthal scales of the instability.

## 7. Conclusion

The von Kármán flows for different values of aspect ratio $\Gamma$ and angular velocity ratio $s$ span a wide variety of instability mechanisms. For our case of $\Gamma = 2$, $s = -1$, the dynamics are dominated by the instabilities of the equatorial shear layer created by the counter-rotating disks. Therefore, the flow is most likely to be unstable to azimuthal equatorial disturbances as was observed in this paper. Neither the radially inward jet due to the recirculation zones nor the sidewall boundary layer seem to play a role. The analysis we have presented provides some evidence that the physical mechanism responsible could be a Kelvin–Helmholtz instability of the equatorial shear layer, complicated by stretching due to the radially inward jet and confinement by the fixed shroud.

The angular velocity ratio $s = \Omega_{up}/\Omega_{low}$ plays an important quantitative role, and determines the symmetry of the configuration as well. The von Kármán rotating disk flows have symmetry group $SO(2)$, the group of rotations about the vertical axis. For $s = -1$, the case studied here, rotation by $\pi$ around the $x$ (or any horizontal) axis is a supplementary invariance, which leads to the richer $O(2)$ symmetry group.

The particular aspect ratio $\Gamma = H/R = 2$ and the quantization of azimuthal wavenumbers along the perimeter have selected two steady states emerging from the axisymmetric basic state: a single vortex associated with the $m = 1$ instability and a co-rotating vortex pair associated with the $m = 2$ instability. These states have similar linear thresholds and compete in a certain range of Reynolds numbers, leading to multiple complex dynamical behaviours: travelling waves and heteroclinic cycles. The transitions between these steady states have been placed in a dynamical systems context: the von Kármán flow with $\Gamma = 2$, $s = -1$, $Re < 500$ is a fluid-dynamical realization of the unfolding of the 1:2 resonance with $O(2)$ symmetry.

We gratefully acknowledge Pascal Chossat for alerting us to the $O(2)$ symmetry of our system; Jean-Luc Guermond and Pierre Lallemand for comparing our numerical results with those from their finite element and Boltzmann codes; and Edgar Knobloch, Isabel Mercader, Jeff Moehlis, Jeff Porter and Joana Prat for sharing their results and insights on near-heteroclinic cycles. The computations were carried out on the NEC-SX5 computer of the Institut du Développement et des Ressources en Informatique Scientifique (IDRIS) of the Centre National pour la Recherche Scientifique (CNRS) (project no. 0254).

## REFERENCES

Armbruster, D. 1987 O(2)-symmetric bifurcation theory for convection rolls. *Physica D* **27**, 433–439.

Armbruster, D., Guckenheimer, J. & Holmes, P. 1988 Heteroclinic cycles and modulated travelling waves in systems with O(2) symmetry. *Physica* D **29**, 257–282.

Aubry, N., Holmes, P., Lumley, J. L. & Stone, E. (1988) The dynamics of coherent structures in the wall region of a turbulent boundary layer. *J. Fluid Mech.* **192**, 115–173.

Barbosa, E. & Daube, O. 2001 A finite differences method in cylindrical coordinates for 3D incompressible flows. *ECCOMAS Computational Fluid Dynamics Conference 2001, Swansea (UK)*.

Batchelor, G. K. 1951 Note on a class of solutions of the Navier–Stokes equations representing steady rotationally-symmetric flow. *Q. J. Mech. Appl. Maths* **4**, 29–41.

Belin, F., Maurer, J., Tabeling, P. & Willaime, H. 1996 Observation of worms in fully developed turbulence. *J. Phys.* II *Paris* **6**, 573–583.

Betchov, R. & Szewczyk, A. 1963 Stability of a shear layer between parallel streams. *Phys. Fluids* **6**, 1391–1396.

Blackburn, H. M. & Lopez, J. M. 2000 Symmetry breaking of the flow in a cylinder driven by a rotating end wall. *Phys. Fluids* **12**, 2698–2701.

Blackburn, H. M. & Lopez, J. M. 2002 Modulated rotating waves in an enclosed swirling flow. *J. Fluid Mech.* **465**, 33–58.

Buzano, E. & Russo, A. 1987 Bifurcation problems with $O(2) + Z_2$ symmetry and the buckling of a cylindrical shell. *Annali di Matematica Pura ed Applicata* (*IV*) **146**, 217–262.

Cadot, O. 1995 Etude des structures de basse pression dans la turbulence développée. PhD thesis, ENS Paris.

Cadot, O., Douady, S. & Couder, Y. 1995 Characterization of the low-pressure filaments in a three dimensional turbulent shear flow. *Phys. Fluids* **7**, 630–646.

Chossat, P. 2001 The bifurcation of heteroclinic cycles in systems of hydrodynamic type. *Dynamics of Continuous, Discrete and Impulsive Systems.* A *Math. Anal.* **8**, 575–590.

Cousin-Rittemard, N., Daube, O. & Le Quéré, P. 1998 Sur la nature de la première bifurcation des écoulements interdisques. *C. R. Acad. Sci. Paris* **326**, 359–366.

Cox, S. 1996 Mode interactions in Rayleigh–Bénard convection. *Physica* D **95**, 50–61.

Crawford, J. D. & Knobloch, E. 1991 Symmetry and symmetry-breaking bifurcations in fluid dynamics. *Annu. Rev. Fluid Mech.* **23**, 341–387.

Dangelmayr, G. 1986 Steady-state mode interaction in the presence of O(2) symmetry. *Dynamics and Stability of Systems* **1**, 159–185.

Daube, O. & Sorensen, J. N. 1989 Simulation numérique de l'écoulement périodique axisymétrique dans une cavité cylindrique. *C. R. Acad. Sci. Paris* **308**, 463–469.

Daube, O., Le Quéré, P., Cousin-Rittemard, N. & Jacques, R. 2001 Influence of curvature on transition to unsteadiness and chaos of rotor–stator disk flows *J. Fluid Mech.* (submitted).

Douady, S., Couder, Y. & Brachet, M. E. 1991 Direct observation of the intermittency of intense vorticity filaments in turbulence. *Phys. Rev. Lett.* **67**, 983–986.

Escudier, M. P. 1984 Observations of the flow produced in a cylindrical container by a rotating endwall. *Exps. Fluids* **2**, 189–196.

Gauthier, G., Gondret, P., Moisy, F. & Rabaud, M. 2002 Instabilities of the flow between co and counter–rotating disks. *J. Fluid Mech.* **473**, 1–21.

Gauthier, G., Gondret, P. & Rabaud, M. 1999 Axisymmetric propagating vortices in the flow between a stationary and a rotating disk enclosed by a cylinder. *J. Fluid Mech.* **386**, 105–126.

Gelfgat, Y. A., Bar-Yoseph, P. Z. & Solan, A. 1996*a* Steady states and oscillatory instability of swirling flow in a cylinder with rotating top and bottom. *Phys. Fluids* **8**, 2614–2625.

Gelfgat, Y. A., Bar-Yoseph, P. Z. & Solan, A. 1996*b* Confined swirling flow simulation using spectral Galerkin and finite volume methods. *FED-ASME* **238**, 105–111.

Gelfgat, Y. A., Bar-Yoseph, P. Z. & Solan, A. 2001 Three-dimensional instability of axisymmetric flow in a rotating lid–cylinder enclosure. *J. Fluid Mech.* **438**, 363–377.

Goda, K. 1979 A multistep technique with implicit difference schemes for calculating two- or three-dimensional cavity flows. *J. Comput. Phys.* **30**, 76–95.

Golubitsky, M., Stewart, I. & Schaeffer, D. G. 1988 *Singularities and Groups in Bifurcation Theory*, vol. 2, Springer.

Haidvogel, D. B. & Zang, T. 1979 The accurate solution of Poisson's equation by expansions in Chebychev polynomials. *J. Comput. Phys.* **30**, 167–180.

Henderson, R. D. & Barkley, D. 1996 Secondary instability in the wake of a circular cylinder. *Phys. Fluids* **8**, 1683–1685.

Hyman, J. M. & Shashkov, M. 1997 Natural discretizations for the divergence, gradient and curl on logically rectangular grids. *Comput. Maths Applic.* **33**, 81–104.

von Kármán, T. 1921 Über laminare und turbulente Reibung. *Z. Angew. Math. Mech.* **1**, 233–252.

Kevrekidis, I. G., Nicolaenko, B. & Scovel, J. C. 1990 Back in the saddle again: a computer assisted study of the Kuramoto–Sivashinsky equation. *SIAM J. Appl. Maths* **50**, 760–790.

Krupa, M. & Melbourne, I. 1995 Asymptotic stability of heteroclinic cycles in systems with symmetry. *Ergod. Theo. Dyn. Sys.* **15**, 121–147.

Labbe, R., Pinton, J.-F. & Fauve, S. 1996 Power fluctuations in turbulent swirling flows. *J. Phys. II France* **6**, 1099–1110.

La Porta, A., Voth, G. A., Moisy, F. & Bodenschatz, E. 2000 Using cavitation to measure statistics of low-pressure events in large-Reynolds-number turbulence. *Phys. Fluids* **12**, 1485–1496.

Lehoucq, R. B., Sorensen, D. C. & Yang, C. 1998 *ARPACK User's Guide*. SIAM, Philadelphia.

Lopez, J. M. 1990 Axisymmetric vortex breakdown. Part 1. Confined swirling flow. *J. Fluid Mech.* **221**, 533–552.

Lopez, J. M. 1996 Flow between a stationary and a rotating disk shrouded by a corotating cylinder. *Phys. Fluids* **8**, 2605–2613.

Lopez, J. M. 1998 Characteristics of endwall and sidewall boundary layers in a rotating cylinder with a differentially rotating endwall. *J. Fluid Mech.* **359**, 49–79.

Lopez, J. M., Hart, J. E., Marques, F., Kittelman, S. & Shen, J. 2002 Instability and mode interactions in a differentially–driven rotating cylinder. *J. Fluid Mech.* **462**, 383–409.

Lopez, J. M., Marques, F. & Sanchez, J. 2001 Oscillatory modes in an enclosed swirling flow. *J. Fluid Mech.* **439**, 109–129.

Lugt, H. J. & Abboud, M. 1987 Axisymmetric vortex breakdown with and without temperature effects in a container with a rotating lid. *J. Fluid Mech.* **179**, 179–200.

Mamun, C. K. & Tuckerman, L. S. 1995 Asymmetry and Hopf bifurcation in spherical Couette flow. *Phys. Fluids* **7**, 80–91.

Marié, L., Burguete, J., Chiffaudel, A., Daviaud, F., Ericher, D., Gasquet, C., Petrelis, F., Fauve, F., Bourgoin, M., Moulin, M., Odier, P., Pinton, J.-F., Guignon, A., Luciani, J. B., Namer, F. & Léorat, J. 2000 MHD in von Kármán swirling flows. *Proc. NATO Dynamo and Dynamics, a Mathematical Challenge, Cargese, France*, pp. 35–50.

Marques, F. & Lopez, J. M. 2001 Precessing vortex breakdown mode in an enclosed cylinder flow. *Phys. Fluids* **13**, 1679–1682.

Marques, F., Lopez, J. M. & Shen, J. 2002 Mode interactions in an enclosed swirling flow: a double Hopf bifurcation between azimuthal wavenumbers 0 and 2. *J. Fluid Mech.* **455**, 263–281.

Mercader, I., Prat, J. & Knobloch, E. 2001 Robust heteroclinic cycles in two-dimensional Rayleigh–Bénard convection without Boussinesq symmetry. *Intl J. Bif. Chaos* **12**, 2501–2522.

Odier, P., Pinton, J.-F. & Fauve, F. 1998 Advection of a magnetic field by a turbulent swirling flow. *Phys. Rev.* E **58**, 7397–7401.

Porter, J. & Knobloch, E. 2001 New type of complex dynamics in the 1:2 spatial resonance. *Physica* D **159**, 125–154.

Proctor, M. R. E. & Jones, C. A. 1988 The interaction of two spatially resonant patterns in thermal convection. Part 1. Exact 1:2 resonance. *J. Fluid Mech.* **188**, 301–335.

Saad, Y. & Schultz, M. H. 1986 GMRES: a generalized minimal residual algorithm for solving nonsymmetric linear systems. *SIAM J. Sci. Stat. Comput.* **7**, 856–869.

Schouveiler, L., Le Gal, P. & Chauve, M.-P. 1998 Stability of a travelling roll system in a rotating disk flow. *Phys. Fluids* **10**, 2695–2697.

Schouveiler, L., Le Gal, P. & Chauve, M.-P. 2001 Instabilities of the flow between a rotating and a stationary disk. *J. Fluid Mech.* **443**, 329–350.

Serre, E., Crespo del Arco, E. & Bontoux, P. 2001 Annular and spiral patterns in flows between rotating and stationary disks. *J. Fluid Mech.* **434**, 65–100.

Serre, E., Hugues, S., Crespo, del Arco, E., Randriamampianina, A. & Bontoux, P. 2001 Axisymmetric and three-dimensional instabilities in an Ekman boundary layer flow. *Intl J. Heat Fluid Flows* **22**, 82–93.

Sotiropoulos, F. & Ventikos, Y. 1998 Transition from bubble-type vortex breakdown to columnar vortex in a confined swirling flow. *Intl J. Heat Fluid Flow* **19**, 446–458.

Sotiropoulos, F. & Ventikos, Y. 2001 The three-dimensional structure of confined swirling flows with vortex breakdown. *J. Fluid Mech.* **426**, 155–175.

Spohn, A., Mory, M. & Hopfinger, E. J. 1998 Experiments on vortex breakdown in a confined flow generated by a rotating disk. *J. Fluid Mech.* **370**, 73–99.

Stevens, J. L., Lopez, J. M. & Cantwell, B. J. 1999 Oscillatory flow states in an enclosed cylinder with a rotating endwall. *J. Fluid Mech.* **389**, 101–118.

Vanel, J. M., Peyret, R. & Bontoux, P. 1986 A pseudo-spectral solution of vorticity – stream-function equations using the influence matrix technique. *Numerical Methods in Fluid Dynamics*, vol. 2. pp. 463–475. Clarendon.

Vogel, H. U. 1968 Experimentelle Ergebnisse über die laminare Strömung in einem zylindrischen Gehaüse mit darin rotierender Scheibe. *Tech. Rep.* **6**, Max-Planck Institute.

Zandbergen, P. J. & Dijkstra, D. 1987 Von Kármán swirling flows. *Annu. Rev. Fluid Mech.* **19**, 465–491.